






Experimental, numerical and analytical evaluation of $\mathbf{j} \times \mathbf{B}$ -thrust for fast-liquid-metal-flow divertor systems of nuclear fusion devices

F. Saenz¹ , A.E. Fisher¹ , J. Al-Salami², B. Wynne¹ , Z. Sun⁷ , T. Tanaka³, T. Kunugi⁴, J. Yagi⁵, K. Kusumi⁵, Y. Wu⁵, G. Yamazaki⁶, C. Hu², K. Hanada² and E. Kolemen^{1,7,*} 

¹ Princeton University, Princeton, NJ 08540, United States of America

² Research Institute for Applied Mechanics, Kyushu University, Fukuoka, Japan

³ National Institute for Fusion Science, Toki, Japan

⁴ Zhejiang University, Hangzhou, Zhejiang 310027, China

⁵ Kyoto University, Kyoto, Japan

⁶ The Graduate University for Advanced Studies, SOKENDAI, Toki, Japan

⁷ Princeton Plasma Physics Laboratory, Princeton, NJ 08540, United States of America

E-mail: ekolemen@pppl.gov

Received 6 June 2023

Accepted for publication 24 July 2023

Published 4 August 2023



CrossMark

Abstract

Divertor systems of fusion devices are exposed to intense heat loads from plasmas, which degrade solid plasma-facing components. Fast liquid metal (LM) flow divertors may be more advantageous for this purpose but have risk of piling due to intense magnetohydrodynamic (MHD) drag. However, severe deceleration of the flow could be countered with the injection of currents that are transverse to external magnetic fields, allowing to thrust the flow with $\mathbf{j} \times \mathbf{B}$ (Lorentz) forces. Given that the injection of currents as an approach to propel LM-divertor flows has remained experimentally understudied, this article focuses on the evaluation of $\mathbf{j} \times \mathbf{B}$ -thrust and finding its drawbacks. $\mathbf{j} \times \mathbf{B}$ -thrust was experimentally tested with free-surface-LM flows, a vertical magnetic field and an externally applied current. Experiments were reviewed with a theoretical model, showing agreement in the trends of theory and experiments. Full 3D-MHD-free-surface-flow simulations were also performed with FreeMHD and confirmed the sensitivity to unstable flow behavior in LM systems when applying external currents. Furthermore, excessive power requirements are expected for the implementation of $\mathbf{j} \times \mathbf{B}$ -thrust at the reactor scale, making these systems inefficient for commercial devices. This paper evidences that the simple operation of a LM-flow divertor with $\mathbf{j} \times \mathbf{B}$ -thrust, without any of the instabilities caused from reactor plasmas or parasitic currents, already presents intrinsic challenges.

* Author to whom any correspondence should be addressed.



Original Content from this work may be used under the terms of the [Creative Commons Attribution 4.0 licence](https://creativecommons.org/licenses/by/4.0/). Any further distribution of this work must maintain attribution to the author(s) and the title of the work, journal citation and DOI.

Keywords: liquid metals, nuclear fusion, 3D-MHD simulation, divertor, magnetohydrodynamics, FreeMHD

(Some figures may appear in colour only in the online journal)

1. Introduction

In magnetic-confinement-fusion devices, the divertor is a plasma-facing component (PFC) that acts as an exhaust system for excessive heat-flux loads from the plasma. These heat loads were predicted to be $\sim 10 \text{ MW m}^{-2}$ without any fusion power released, and it is expected to increase up to $\sim 31 \text{ MW m}^{-2}$ for ITER in H-mode operation [1]. These heat loads cause surface degradation of solid PFCs, and could dramatically reduce their lifetime to the order of hours [2]. Current designs of solid PFCs require further developments to withstand such extreme conditions.

LM-free-surface flows may address the aforementioned shortcomings of solid PFCs as they offer: (1) higher heat-transfer rates through convection and phase-change processes, (2) immediate material replenishment after plasma disruptions, (3) elimination of net-reshaping of the PFCs due to plasma erosion and or redeposition [3], (4) potentially decreasing the erosion lifetime requirements to $\sim 10 \text{ s}$ – 100 s as LMs are constantly replenished [4, 5], among others. Nevertheless, while the application of LMs in divertors and blankets is promising to handle the heat loads in future nuclear fusion reactors, the present knowledge and applications of LM flows in these environments is rather poor.

The concept of fast flows for divertors has been considered previously for the design of a divertor in the Fusion Nuclear Science Facility (FNSF) [6] and the Flowing Liquid Torus (FLIT) [7]. However, none of these reports addressed the methods to achieve the flow speeds required to avoid LM overheating. Previous studies have proposed the application of external currents to control LM flows, like the Active Radiative Liquid Lithium Divertor concept [8], Magnetic Propulsion [9], and divertorlets [10, 11]. However, this topic has remained experimentally understudied, as only the operational principle of the divertorlets concept has been tested. For the previous reasons, it is necessary to experimentally test the applicability of thrust-generation approaches in LM flows for divertor solutions.

1.1. Critical flow speeds for heat exhaust

LM divertors could suffer excessive evaporation due to large heat loads. Thus, the maximum permissible temperature of the LM defines the heat flux q_{\perp} that could be exhausted by an LM-PFC. The relation between the temperature of a free-surface-LM flow and the heat flux can be established with a semi-infinite slab model [12]. Figure 1 depicts a simplified diagram of a LM slab flowing under a heat-flux load.

The heat-flux load q_{\perp} impinges on the free surface of the liquid metal, either a neutron-wall load or the heat flux in the divertor region. L is the distance along which the liquid metal is exposed to the heat-flux load from the reactor plasma and

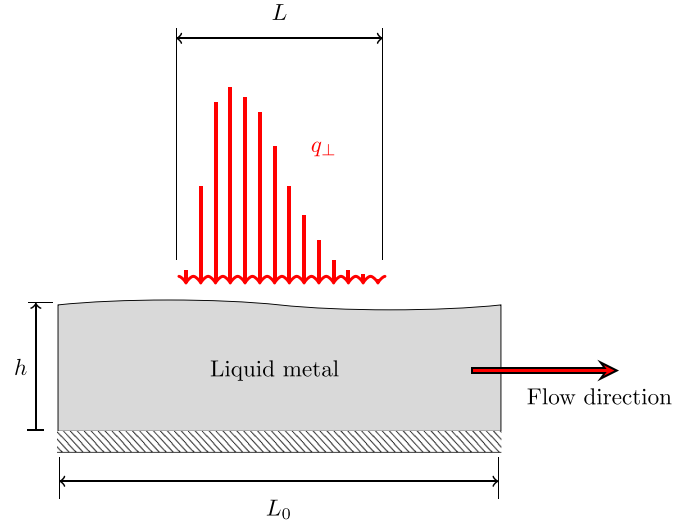


Figure 1. Schematic of plasma heat flux on flowing liquid metal.

v is the bulk speed of the liquid metal. If the thickness of the LM flow is assumed to be larger than the thermal penetration depth $d_{th} = \sqrt{\frac{tk}{c}}$, where t is the exposure time of the LM to q_{\perp} , and c and k are heat capacity and thermal conductivity of the LM, respectively, then the temperature increase $\Delta T(t)$ at the free surface of the LM is approximated with equation (1) [12]

$$\Delta T(t) = 2 \frac{q_{\perp}}{k} \sqrt{\frac{\alpha t}{\pi}}. \quad (1)$$

In equation (1), α is the thermal diffusivity of the LM. t can be approximated as $t = \frac{L}{v}$. To avoid LM overheating/evaporation, a critical LM-free-surface temperature increase ΔT_{cr} is defined. The critical flow speed v_{cr} is the required minimum flow speed for the LM flow to avoid surpassing a critical temperature increase ΔT_{cr} at a given heat-flux load

$$v_{cr} = \frac{4\alpha L}{\pi} \left(\frac{q_{\perp}}{k\Delta T_{cr}} \right)^2. \quad (2)$$

For ITER, L is approximated as $2\lambda_q$, where λ_q corresponds to the heat-flux width, thus $L \sim 0.5$ – 5 cm [2, 13, 14]. For the case of liquid lithium: $\rho = 516 \text{ kg m}^{-3}$, $k = 45 \text{ W (m}\cdot\text{K)}^{-1}$, $\sigma = 3.341 \text{ MS m}^{-1}$, $\mu = 0.5 \cdot 10^{-3} \text{ Pa}\cdot\text{s}$, $c = 4169 \text{ J (kg}\cdot\text{K)}^{-1}$ [15]. With the aforementioned parameters, the critical speed for a linear-flow divertor configuration of liquid lithium is $v_{cr} \sim 1$ – 20 m s^{-1} . Other LMs like tin, lithium, tin-lithium eutectic mixtures, and gallium would require speeds of the same order of magnitude and a flow thickness of 1 – 20 mm [4, 16, 17].

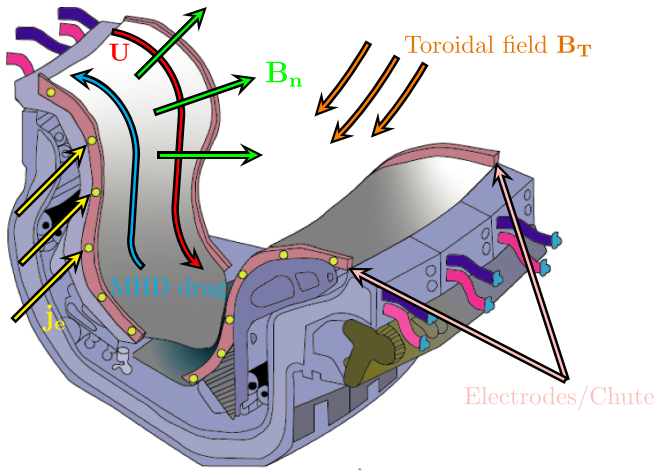


Figure 2. Top view of a sample cassette arrangement in a divertor of a tokamak.

The $1\text{--}20\text{ m s}^{-1}$ speed range corresponds to the ‘fast’ flow operating regime. The difference between the fast and slow regimes is that fast flows are intended to operate as the main heat removal system, and slow flows are mainly for the protection of PFCs against erosion and they require a heat removal system [7] for the solid substrate. The focus of this work is fast LM flows for divertors and a potential method to overcome issues related to magnetohydrodynamic (MHD) drag in a reactor.

1.2. $\mathbf{j} \times \mathbf{B}$ -thrust

Electrically conductive flows in divertors are subject to transverse magnetic fields, which generates currents in the LM and causes MHD drag in LM flows. This force decelerates the flow and causes LM pileups. This issue is greatly exacerbated for fast-flow PFCs as MHD drag $\sim (\mathbf{U} \times \mathbf{B}) \times \mathbf{B}$ is proportional to the velocity field \mathbf{U} of the LM flow. Furthermore, MHD drag forces could increase depending on the dimensions and electrical conductivity of the boundaries around the LM flow.

However, MHD drag forces could be countered with the application of external transverse electric currents that generate $\mathbf{j} \times \mathbf{B}$ thrust [3, 14] on a free-surface-liquid-metal flow (FSLMF). This mechanism may also be applied to oppose any $\mathbf{j} \times \mathbf{B}$ forces created by plasma currents. By taking advantage of the ‘cassette’ configuration for divertors of ITER-like reactors [18] and the surface-normal magnetic field \mathbf{B}_n , a potential solution is the use of electrodes on either side of these cassettes, and passing electric currents across the flow (see figure 2).

For reactor operation, the $\mathbf{j} \times \mathbf{B}$ -thrust from external currents could be used to avoid LM pileups in the system. This can be achieved by applying $\mathbf{j} \times \mathbf{B}$ -thrust forces of the same order of magnitude to the MHD-drag forces expected. The application of far larger $\mathbf{j} \times \mathbf{B}$ -thrust forces, while attractive for fast flow concepts, may aggressively accelerate the liquid and lead to hydraulic-jump-like discontinuities. Such jumps are undesirable since they can significantly slow down the

flow and lead to the formation of hot spots due to abrupt deformations in the shape of the free-surface. Additionally, excessive acceleration of the flow may cause flow detachment from the sidewalls of the cassette/chute, which would leave portions of the substrate beneath the LM flow exposed to the plasma.

According to the latter requirements for operation of LM systems, ‘achieving $\mathbf{j} \times \mathbf{B}$ -flow propulsion’ is defined for purposes of this article as obtaining steady flows (with no hydraulic-jump-like discontinuities and no flow detachment from the side walls) along the section where an external transverse current \mathbf{j}_e is injected, and these flows must also show increasing flow speed with increasing \mathbf{j}_e at a constant \mathbf{B}_n .

In order to analyze $\mathbf{j} \times \mathbf{B}$ -thrust on FSLMFs, experiments were performed with a vertically oriented magnetic field (mimicking a surface-normal field \mathbf{B}_n in a reactor) and transversely injected electric currents on LMs. Tests were executed using the Oroshhi-2 superconducting magnet of the National Institute for Fusion Science (NIFS), with LM flows in the LM-Free-surface-Experiment (LMFREX) channel from Kyoto University.

Two types of experiments were performed: $\mathbf{j} \times \mathbf{B}$ -thrust and $\mathbf{j} \times \mathbf{B}$ -counterthrust. These tests allowed the imitation of the magnetic field conditions of a reactor scenario and the evaluation flow propulsion and counter-propulsion while observing subsequent issues during operation. In this paper, the setup used for experiments and diagnostics is described. The results from experiments and a respective analysis for each type of test, using equations of the shallow-free-surface-flow model (SFSFM), are shown.

Finally, simulation results with a recently developed tool called FreeMHD [19] are also shown for these tests, showing agreement with the simplified analytical equations derived. More experimental validation of FreeMHD is found here [20]. The aim of this work is beyond finding the required flow speeds to avoid overheating in LM-divertor systems. It evaluates the implementation of $\mathbf{j} \times \mathbf{B}$ -thrust as a mechanism for propulsion in LM flows under extreme MHD drag forces, and it identifies its drawbacks at the reactor scale.

2. Methodology

2.1. Experiments

All tests described were executed in the LMFREX channel of Kyoto University (see figure 3(a)) [21, 22]. LMFREX is an acrylic channel equipped with a heater and thermocouple array to study heat flux within MHD flows. The LMFREX channel was brought to NIFS and was placed below the superconducting magnet of the Oroshhi-2 facility, in a region of approximately 40% of the core field strength (see figure 3(b)).

The Oroshhi-2 facility also has a LM-flow loop that runs PbLi and FLiNaK in pipes or ducts through a 3 T superconducting magnet to study MHD effects on the flow [23, 24]. For experiments shown in this article, $|\mathbf{B}_n|$ had a maximum of 1.4 T. As a note, $|\mathbf{B}_n|$ in the divertor region for an LM-PFC would be smaller than $0.05|\mathbf{B}_T|$. For the case of ITER,

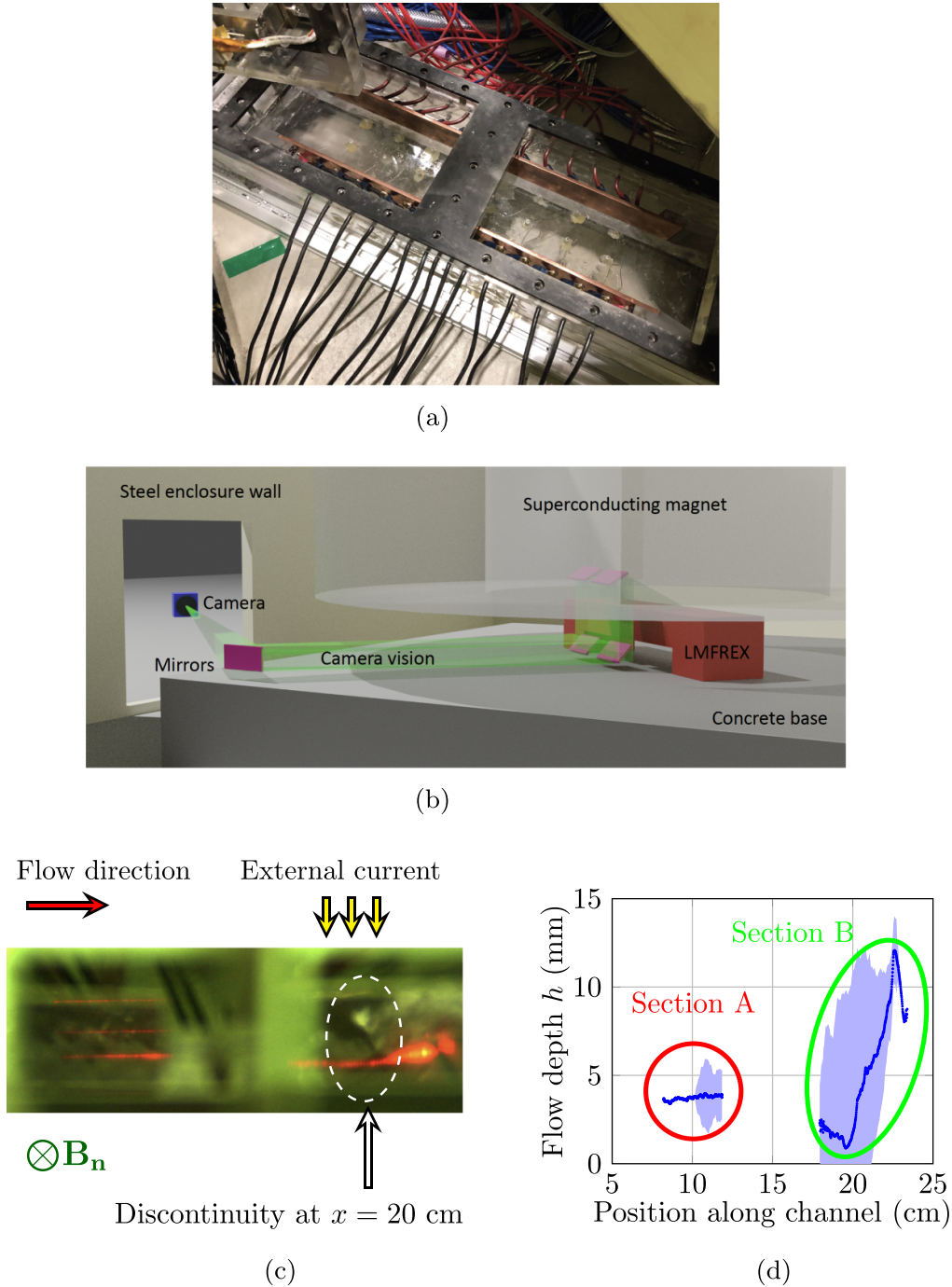


Figure 3. Data processing from laser sheet recording to a flow depth profile. (a) The LMFREX channel with wall electrodes. Notes: the electrode test section is 8 cm wide, and 30 cm long. (b) Experimental setup showing camera and mirror array—the laser sheet used separate mirrors shined vertically down. (c) Projection of laser-sheet (red line) on the LM free surface. Flow direction is from left to right. Frame taken from a recording of an experiment with a hydraulic-jump-like behavior. Processed data for this experiment are shown in figure 3(d). (d) Processed h -data from laser on figure 3(c). The dark-blue line represents the experimental measurement. The light-blue shading represents the local variance for the measurement.

$|\mathbf{B}_n| < 0.1$ T, therefore MHD effects from surface-normal fields were up to those found in ITER and beyond.

For the experiments performed, the liquid metal alloy commercially known as galinstan (GaInSn) was used as the working fluid, (67% Ga, 20.5% In and 12.5% Sn). Properties of galinstan are $\rho = 6360 \text{ kg m}^{-3}$, $k = 296 \text{ W (m}\cdot\text{K)}^{-1}$, $\sigma = 3.1 \text{ MS m}^{-1}$, $\mu = 0.0019 \text{ Pa}\cdot\text{s}$, $c = 366.5 \text{ J (kg}\cdot\text{K)}^{-1}$

[25, 26]. During experiments, argon gas was pumped inside the LMFREX channel to prevent the oxidation of the LM. An experimental $\mathbf{j} \times \mathbf{B}$ -pump was used to circulate the LM.

In particular, for some $\mathbf{j} \times \mathbf{B}$ -thrust experiments, the LM flow suffered flow detachment from the electrodes. Ensuring full coverage of the bottom wall of the channel and full contact with the electrodes was required during experiments for

further analysis. To achieve this, the initial infill level of the LMFREX channel was increased until this requirement was met. As a note, depending on the infill level and the flow rate, a pile of LM was generated as the outlet of the channel could not evacuate enough flow, and the wall at the end of the channel acted as a flow barrier.

For the application of external currents in LMFREX, two copper electrodes were installed on either side of the channel, working as positive and negative electrodes. The electrodes were 1/8" thick \times 1" tall \times 12" long. The maximum height of the LM surface was just below 2 cm during all experiments.

Each of the electrodes had a set of 15 wire connections spaced by 2 cm to ensure the uniformity of the injected electric current. Each of the 15 wires was connected to a larger single cable. Experimental measurements showed that each wire carried the same amount of current within a few percent. The maximum total current applied during experiments was 150 A.

Flow depth measurements were performed with a laser sheet incident on the surface of the LM. This diagnostic has been used as a non-intrusive height measurement [27]. Due to the large magnetic field strengths of the Oroshhi-2 superconducting magnet, the camera and laser sheet were kept at a distance outside of the magnetic shield and operated through viewing ports. A two-mirror setup was used to reflect the laser sheet on the LM. A three-mirror setup allowed video recordings of the motion of the laser sheet with optical measurements using a CCD camera far from the core of the magnet. Figure 3(b) shows an representation of the mirror setups.

For all tests, there were two sections of the LMXFREX channel, henceforth referred to as sections A and B, where a laser sheet was projected upon the LM surface. Section A was closer to the inlet and section B was closer to and outlet of the LMFREX channel. The orientation of the laser-sheet diagnostic is shown in figure 3(c), also with a sample imaging of a hydraulic-jump-like behavior during an experiment in figure 3(d). For clarification purposes, the flow direction is 'from left to right' in all figures shown.

The flow-depth measurements shown in this paper were time-averaged from the laser-sheet data obtained. The shaded areas behind each h -profile represent the error bars of the respective profile. The magnitude of the error is determined by the thickness laser-sheet projection on the free surface of the LM flow. In general, this projection remained steady for all experiments, except for those with hydraulic-jump-like discontinuities. The parameters that were varied between experiment runs were: flow rate, magnetic field strength, externally injected electric current, as well as the initial LM fill level.

2.2. Shallow-free-surface-flow model

The SFSFM is derived from simplifications shown in [28]. It has been used to study hydraulic-jump experiments in narrow channels [29] and to find critical heights of flows under transverse magnetic fields [30]. A different formulation was used to study the effect of viscous shear on free surface flows and the generation of natural hydraulic-jump-like discontinuities [31]. More recently, SFSFM was reformulated to understand

the effect of channel inclination on flows [32–35]. The specific approach followed in this article is presented in [36], with variations added to describe $\mathbf{j} \times \mathbf{B}$ -forces in the flow. The complete derivation is in appendix A.

One of the main assumptions of the SFSFM model is 'steady-state' flows, which indeed sets a constraint on the flow regime (laminar or turbulent) that is possible to analyze. However, the reader is reminded that the SFSFM was used in this article to describe either flows that were steady (determined by a steady free surface) or flows that were 'quasi-steady' (determined by waves on the surface whose amplitude does not grow in time). The SFSFM is primarily used to study the trends observed in experiments and to identify leading-order body forces that govern the flow behavior.

2.3. Simulation setup

SFSFM may oversimplify the flow analysis in some cases. In particular, the reduction to a single-dimension flow ignores the presence of stream-wise components of the applied current. The latter could cause three-dimensional behavior that is impossible to describe through SFSFM. In order to study such effects, 3D simulations were carried out using FreeMHD [19], which is a solver developed in the framework of the OpenFOAM CFD toolbox [37].

FreeMHD was previously validated with experiments under different conditions that alter MHD drag forces in a LM flow [20] subject to a toroidal magnetic field. For this work, further validation of FreeMHD is shown for magnetic fields normal to the free surface of the flow and externally applied currents. For this purpose, different electrical currents were applied to the LM flow (generating $\mathbf{j} \times \mathbf{B}$ -thrust and $\mathbf{j} \times \mathbf{B}$ -counterthrust).

Indeed, $\mathbf{j} \times \mathbf{B}$ -counterthrust experiments are not relevant to divertor scenarios. Nevertheless, FreeMHD is a recently developed tool and validating this simulation code under different MHD conditions is necessary. Moreover, it improves the reliability of the results when making projections at the reactor scale with this tool. Details about governing equations and boundary conditions used in FreeMHD are in appendix B.

3. Results and discussion

3.1. Analysis of experiments through SFSFM and simulations

SFSFM was used to analyze the evolution of the flow-depth profile for experiments with different body forces. The solutions were obtained by using the first data point (x_1, h_1) from section A (see figure 3(d)), and iterating a value of λ_1 at this respective position such that the theoretical solution satisfies the condition of the last data point of section A or a data point in section B (x_2, h_2) . The purpose of this analysis is to identify the leading forces that determine the behavior of the flow under externally applied currents.

Moreover, in order to validate FreeMHD solver for the flows studied in this paper, 3D simulation results were compared to experimental data and SFSFM. Notice that the height of the LM surface was not fixed in all simulations shown in

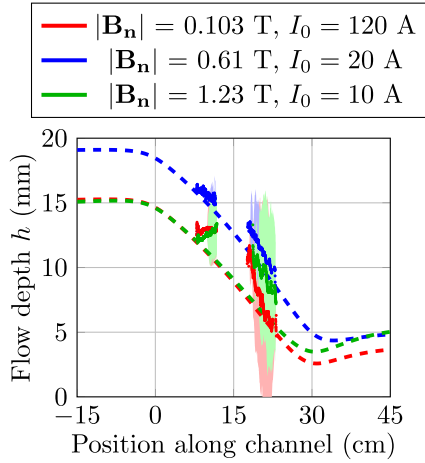


Figure 4. h -profiles for $\mathbf{j} \times \mathbf{B}$ -thrust experiments. $Q = 0.7 \text{ L min}^{-1}$ for all experiments shown. $k = 0$ for all plots shown. Dashed lines represent the results from SFSFM, dots correspond to experimental results. Shaded areas represent the error bars from experimental measurements.

this section and that only the physical parameters of the LM, channel geometry, flow rate Q , externally applied current I_0 and magnetic field \mathbf{B} were specified.

3.1.1. $\mathbf{j} \times \mathbf{B}$ -counterthrust. Experimental results for three different $\mathbf{j} \times \mathbf{B}$ -counterthrust experiments are shown in figure 4. The LM flow piled up near the inlet during the experiments due to flow deceleration. Results from the momentum equation are shown in figure 4 and the agreement with the experiment data is observable. The velocity profile variation and magnitudes of the forces for one of the $\mathbf{j} \times \mathbf{B}$ -counterthrust experiments are shown in figure 5.

From figure 5(b), it is noticeable that the leading forces are $-\nabla p$ and $\mathbf{j}_e \times \mathbf{B}$, while all other forces could be considered negligible, at least for $0 \text{ cm} < x < 30 \text{ cm}$, which is the test section. Equation (3) shows this simplification, and it is obtained after rewriting the force balance from equation (9) while ignoring advection, MHD drag and viscous drag from equation (10)

$$0 \approx -g \frac{\partial h}{\partial x} + \frac{j_e B}{\rho} \Rightarrow \frac{\partial h}{\partial x} \approx \frac{j_e B}{\rho g}. \quad (3)$$

From the balance between hydrostatic pressure and $\mathbf{j}_e \times \mathbf{B}$, it is clear that the flow-depth slope varies according to the magnitude and sign of the external current density j_e . A ‘negative’ electric current was applied in the experiments shown in figure 4, consistent with the negative slope obtained for the h -profile in figure 5(a). 3D simulation results shown in figure 5(a) are also in agreement with both experimental and SFSFM results.

3.1.2. $\mathbf{j} \times \mathbf{B}$ -thrust. Experimental results for three different $\mathbf{j} \times \mathbf{B}$ -thrust experiments are shown in figure 6. Results from the momentum equation are also shown in figure 6 for each respective experiment. The theoretical h -profiles in figure 6

were calculated while ensuring a continuous solution for λ in the range shown for each plot. There is a disagreement between the slopes of the h -profiles obtained from theoretical plots and experimental results. As previously mentioned, the experimental results are affected by the initial infill level of liquid metal. Furthermore, 3D-effects from external and induced currents were present during these experiments, and they are not being considered in the SFSFM. This will be addressed in section 3.2.

Moreover, the variation of the velocity profile and magnitudes of the forces for the $|\mathbf{B}_n| = 0.103 \text{ T}$, $I_0 = 22 \text{ A}$ experiment are shown in figure 7. In addition, a comparison with a simulation result from FreeMHD shows agreement with results from experiments and SFSFM.

From figure 7(b), the leading-order forces are $-\nabla p$ and the $\mathbf{j}_e \times \mathbf{B}$ for $0 \text{ cm} < x < 30 \text{ cm}$, and all other forces could be considered negligible. Equation (4) shows this simplification, and it is obtained after rewriting the force balance from equation (9) while ignoring the advection, MHD drag and viscous drag from equation (10)

$$0 \approx -g \frac{\partial h}{\partial x} + \frac{j_e B}{\rho} \Rightarrow \frac{\partial h}{\partial x} \approx \frac{j_e B}{\rho g}. \quad (4)$$

The result in equation (4) indicates that the flow-depth slope varies according to the magnitude and sign of the external current density j_e . For the experiment shown in figure 6, a positive electric current was applied, confirming the positive slope obtained for the h -profile.

In general, the $\mathbf{j} \times \mathbf{B}$ -thrust experiments performed were not able to show flow propulsion with the injection of external currents. The experimental setup was sensitive to the parameters used to run experiments: initial infill of LM, magnetic field intensity, external current applied, etc. Small initial infills of LM in the channel lead to empty channel after the application of $\mathbf{j} \times \mathbf{B}$ -thrust. However, experiments with increased initial infill forced the occurrence of hydraulic-jump-like discontinuities, as the channel was not able to pump out enough LM.

3.1.3. Hydraulic-jump-like behavior. For $\mathbf{j} \times \mathbf{B}$ -thrust experiments with magnetic flux densities smaller than 0.3 T and currents above 60 A, a hydraulic-jump-like behavior was generated, and it depended mainly on the magnitude of the applied current. Figure 8 illustrates the result of an experiment with said phenomenon. As a note, the LM flow did not detach from the side walls of the chute during the experiment. Moreover, contrary to the positive-slope h -profiles shown for $\mathbf{j} \times \mathbf{B}$ -thrust experiments, tests with hydraulic-jump-like discontinuities did show accelerating flows (decreasing depth of the flow) before the discontinuity.

The nature of the ‘discontinuity’ in figure 8(a), is not completely captured by SFSFM. A first cause is the fact that not enough LM was drained from the LMFREX channel during the experiment, which caused a pile of LM near the outlet and forced a hydraulic jump. A second cause is related to three-dimensional effects of the injected current, as shown in section 3.2 through FreeMHD simulations.

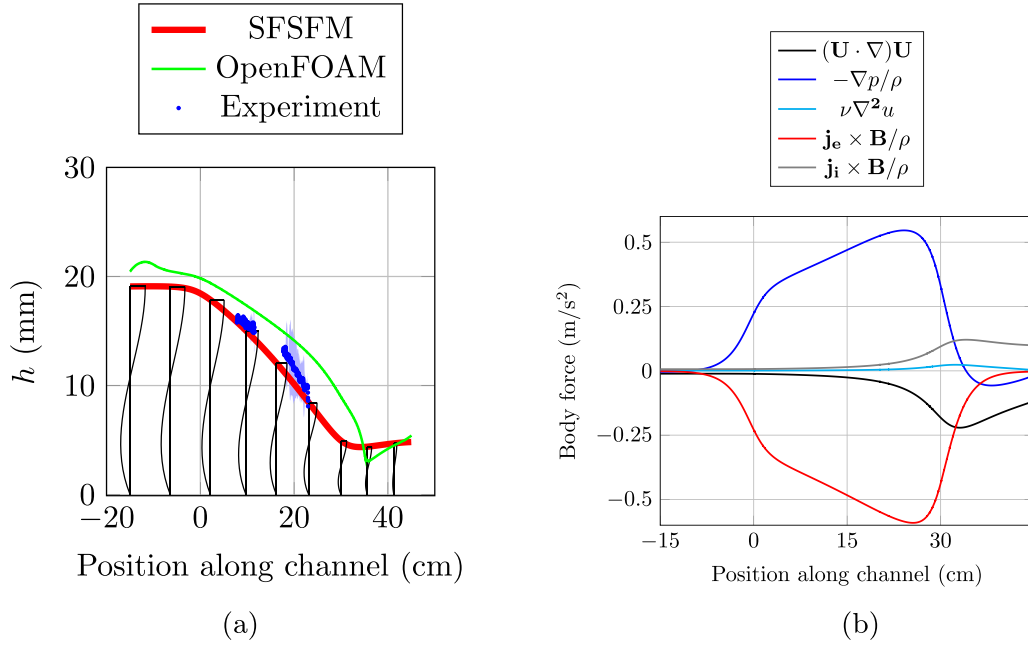


Figure 5. $\mathbf{j} \times \mathbf{B}$ -counterthrust experiment. $Q = 0.7 \text{ L min}^{-1}$, $I = 20 \text{ A}$, $B = 0.61 \text{ T}$. (a) Height profile and velocity profile variations on stream-wise direction. Note: black lines show the shape of the local velocity profile. Black vertical lines indicate the positions of the velocity profiles shown. (b) Body forces and acceleration terms in the stream-wise direction.

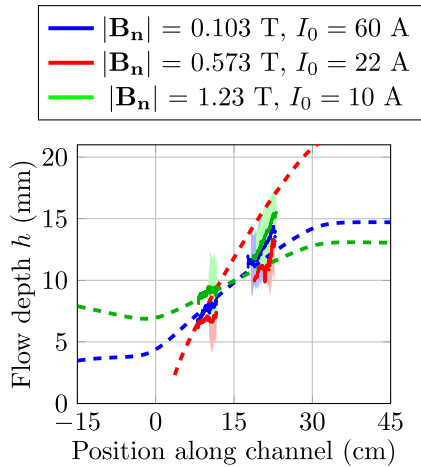


Figure 6. h -profiles for $\mathbf{j} \times \mathbf{B}$ -thrust experiments. $Q = 1.9 \text{ L min}^{-1}$ for all experiments shown. Dashed lines represent the results from SFSFM, dotted plots correspond to experimental results. Shaded areas represent the error bars from experimental measurements. $k = 0$ for all plots shown.

3.2. Three-dimensional effects of electric currents

3.2.1. Galinstan flows on an insulated substrate. One issue observed during experiments was flow detachment from the side walls, as shown in figure 9. This detachment was caused either by excessive thrust on the LM flow, or due to fringing effects of the applied current. Another issue observed was the hydraulic-jump-like behavior, which was also generated by these fringing currents. These two issues caused by fringing currents were studied through FreeMHD simulations with the inclusion of three-dimensional currents.

Figure 10 shows results from a FreeMHD simulation carried out to analyze the effect of small initial infill levels on the flow and the flow barrier at the end of the channel. Figure 10(a) shows the fringing effect of the externally applied current near the upstream (left) and downstream (right) edges of the electrodes.

Given the direction of \mathbf{B}_n (into the page), the $\mathbf{j} \times \mathbf{B}$ force near the upstream edges pinches the flow away from the electrodes and towards the center line of the channel. This pinching action eventually causes the film to detach from the electrodes and form a rivulet-type flow (see figure 10(b)). Near the downstream edges of the electrodes, the fringing \mathbf{j}_e has the opposite effect, pushing the liquid away from the center line of the channel towards the side walls, consequently leaving portions of the substrate uncovered by LM.

Once the flow detaches from both side walls near the upstream (left) electrode edges, the conduction of the electric current is sensitive to the shape of the LM flow on the $x-y$ plane. The rivulet-type flow forces the current to be carried in the stream-wise direction, and this generates a net force that pushes the flow to one of the electrode walls (see figure 10(c)). Finally, an unsteady flow was obtained, the flow mainly attached to one electrode and left some sections of the substrate uncovered by LM (see figure 10(d)).

As previously mentioned, flow detachment observed in initial $\mathbf{j} \times \mathbf{B}$ -thrust experiments was eliminated by increasing the initial infill of LM, which decreased the magnitude of \mathbf{j}_e in the LM, thus reducing the $\mathbf{j} \times \mathbf{B}$ -pinch force near the edges of the electrodes. Moreover, increasing the infill level also prevented the channel from being excessively emptied by abrupt flow propulsion and the exposure of the substrate beneath the LM flow.

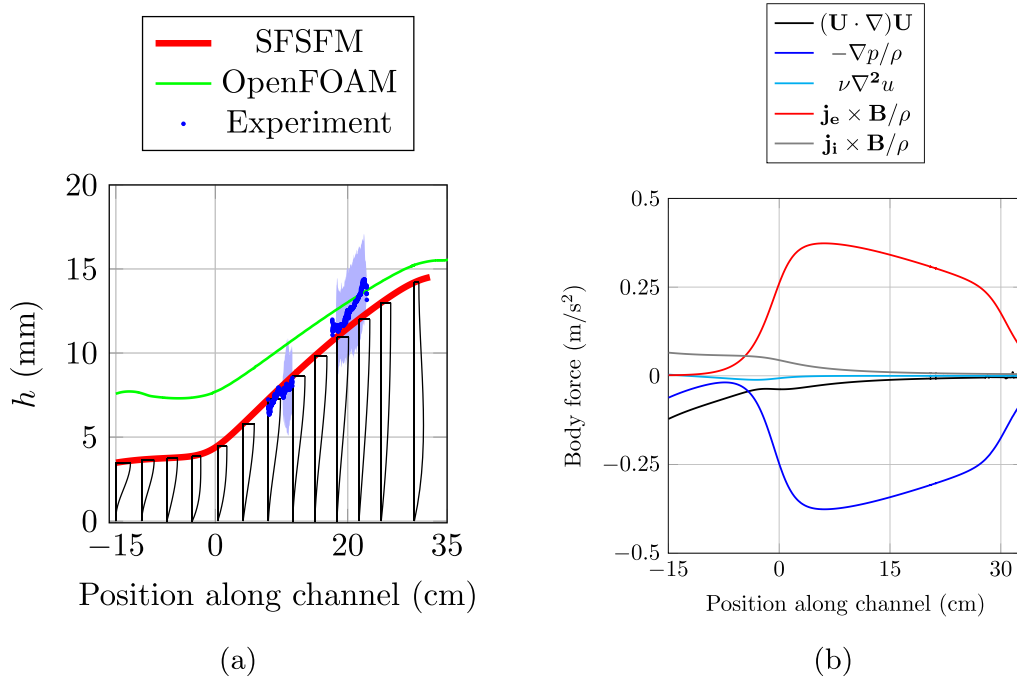


Figure 7. $\mathbf{j} \times \mathbf{B}$ -thrust experiment: $Q = 1.9 \text{ L min}^{-1}$, $I = 60 \text{ A}$, $|\mathbf{B}_n| = 0.103 \text{ T}$. (a) Height profile and velocity profile variations on stream-wise direction. Note: black lines show the shape of the local velocity profile. Black vertical lines indicate the positions of the velocity profiles shown. (b) Body forces in stream-wise direction.

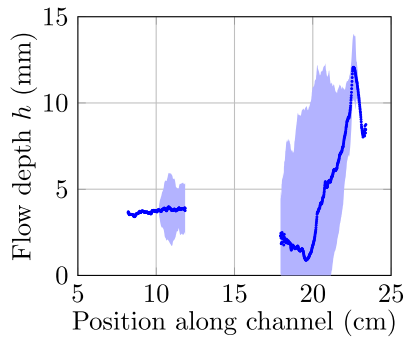


Figure 8. $\mathbf{j} \times \mathbf{B}$ -thrust experiment. $Q = 1.9 \text{ L min}^{-1}$, $I = 120 \text{ A}$, $|\mathbf{B}_n| = 0.0821 \text{ T}$.

However, after increasing the initial infill level, the flow either generated a pile of LM near the outlet of the channel (which is caused by a balance between $\mathbf{j} \times \mathbf{B}$ -thrust and $-\nabla p$, as explained in section 3.1.2) or forced a hydraulic-jump-like behavior. The latter occurred because the outlet of the channel was not adequate to extract enough LM flow and prevent these issues. Thus, flow propulsion was not experimentally proven.

In order to analyze possible flow propulsion with external currents, simulations were performed to evaluate the effect of an outlet that eliminated LM accumulation in the channel (see figure 11). Rather than limiting the outflow rate to be equal to the inflow, a boundary condition that allows the LM to exit the domain freely as if it were falling off a waterfall was used.

In figures 11(a) and (b), the result of \mathbf{j}_e -fringing effects is visible before the flow enters the region with electrodes

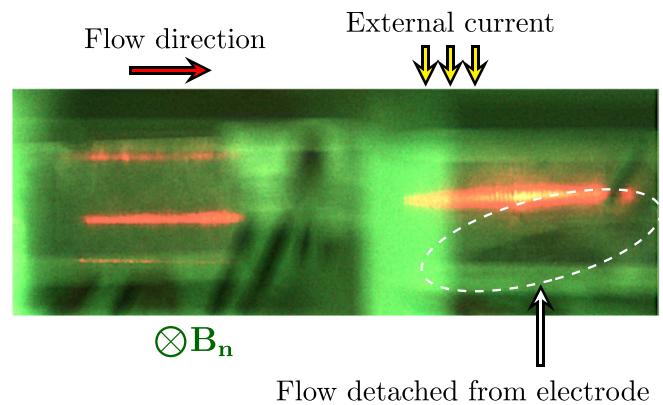


Figure 9. Experimental result for $I_0 = 60 \text{ A}$, $|\mathbf{B}_n| = 0.103 \text{ T}$, $Q = 1.9 \text{ L min}^{-1}$.

($x < 15 \text{ cm}$), as the flow is pinched away from the electrodes towards the center of the channel. Also, even with an outlet condition that prevents LM accumulation, there is a drastic increase in the LM depth after the flow leaves the electrode region ($x > 45 \text{ cm}$, see figure 11(c)). While similar to a hydraulic-jump-like behavior, the flow is simply being pushed away from the center line of the channel due to \mathbf{j}_e -fringing effects. This behavior is not desired if a heat flux load is present on the free surface of the LM flow, as it would fastly heat the regions with thinner LM flow films.

Figure 11(c) also shows that an increasing $\mathbf{j}_e \times \mathbf{B}$ -thrust force did achieve flow propulsion without LM pileups and jump discontinuities, as h decreased in the middle of the region with electrodes after increasing I_0 from 10 A to 20 A. In order

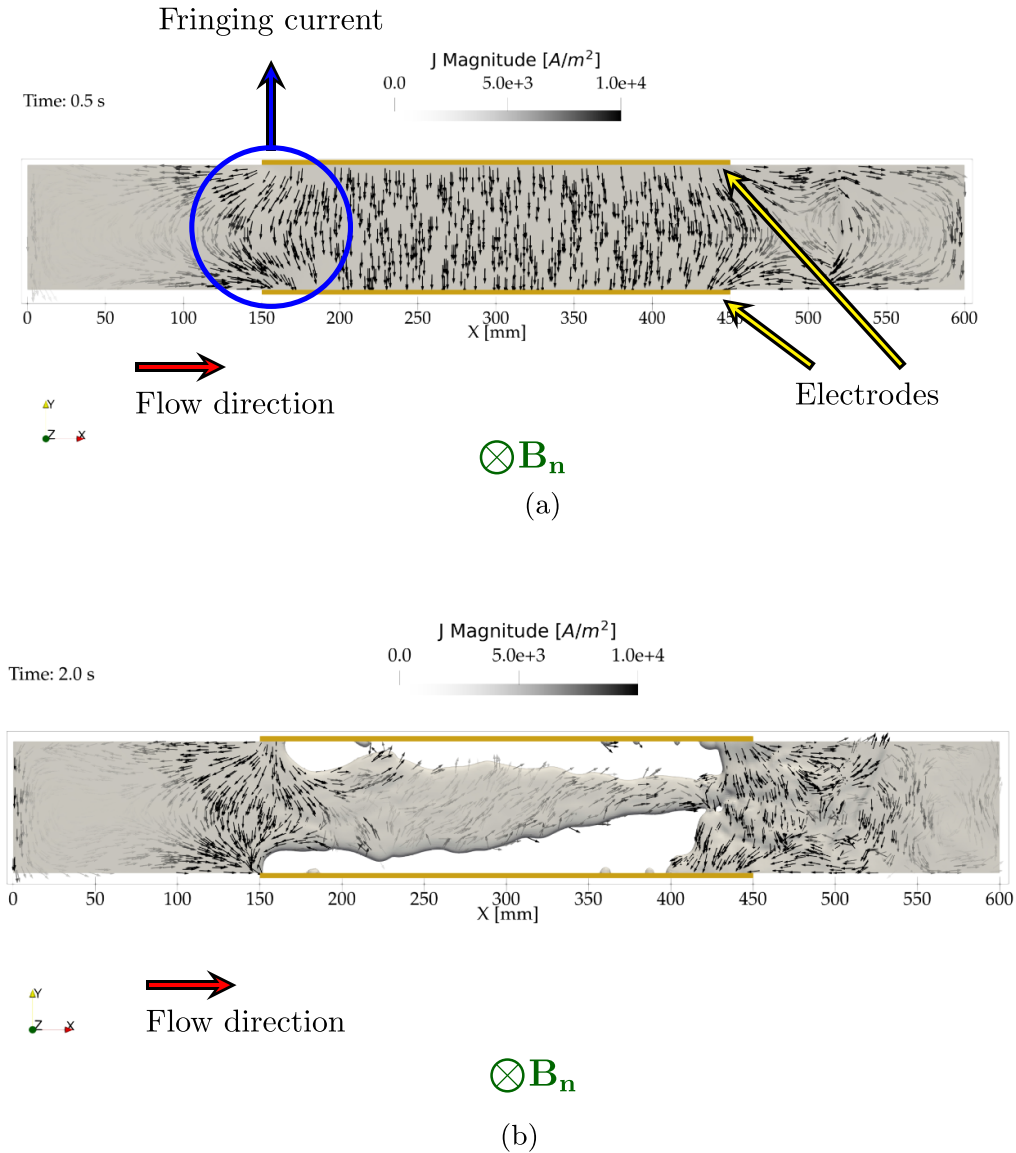


Figure 10. Simulation result for $I_0 = 60$ A, $|\mathbf{B}_n| = 0.103$ T, $Q = 1.9$ L min $^{-1}$. Note: black arrows in (a)–(c) represent the direction density field of the injected current \mathbf{j}_e . (a) Top view of the LMFREX channel during simulation showing fringing current density \mathbf{j}_e . Note: the black-arrow field indicates the direction of the externally applied current in the LM flow. (b) Top view of the LMFREX channel during simulation showing flow detachment from side walls due to fringing effects of external current. Note: the black-arrow field indicates the direction of the externally applied current in the LM flow. (c) Top view of the LMFREX channel during simulation anomalous conduction of external current. Note: the black-arrow field indicates the direction of the externally applied current in the LM flow. (d) Bottom substrate not covered by LM due to unsteady flow.

to confirm flow propulsion with $\mathbf{j}_e \times \mathbf{B}$ -thrust and to avoid \mathbf{j}_e -fringing effects, more simulations were executed with an insulating substrate for the bottom surface of the channel (see figure 12). The electrodes for these simulations were as long as the channel (0.6 m).

3.2.2. $\mathbf{j} \times \mathbf{B}$ -thrust on lithium flows in an inclined magnetic field. The analysis previously shown only accounted for the effect of a surface-normal magnetic field. However, in a realistic reactor environment, a toroidal magnetic field component \mathbf{B}_T would also be present. To study the efficacy of $\mathbf{j} \times \mathbf{B}_n$ -thrust under the influence of an inclined magnetic field,

simulations were carried out with $|\mathbf{B}_T| = 1$ T and $|\mathbf{B}_n| = 0.1$ T, as shown in figure 13.

The relative magnitudes of the horizontal and surface-normal components were chosen to mimic those found in the divertor region. To avoid undesirable fringing current effects from previous sections (see figure 10(a)), the electrodes were extended along the entire length of the channel in all simulations shown in this section. Additionally, the operating liquid metal was changed to liquid lithium, as it is more desirable for reactor operation.

Figure 13(a) shows that flow propulsion was achieved with $I_0 = 50$ A in an electrically-insulated substrate. However, in figure 13(b), it is shown how an accelerating flow due

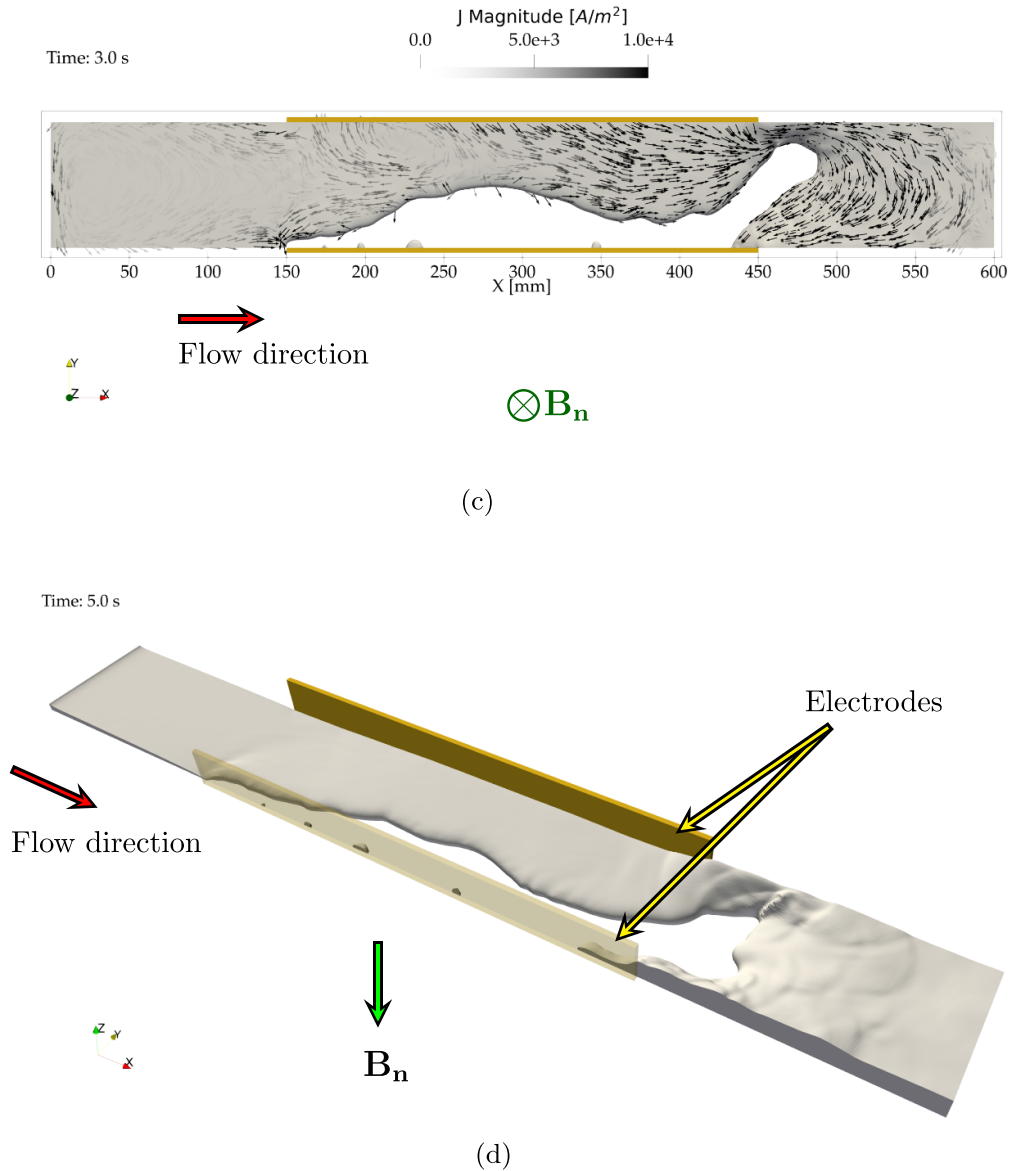


Figure 10. (Continued.)

to $\mathbf{j}_e \times \mathbf{B}$ -thrust suffers from induced stream-wise currents, which push the liquid to one side of the channel. This adverse side effect is the result of a flow-velocity stream-wise gradients caused by the acceleration of the flow, which consequently creates a gradient in the $\mathbf{U} \times \mathbf{B}$ field and in the electric potential.

The latter effect is undesirable for reactor operation as it could lead to flow detachment and the instabilities previously mentioned and shown in figure 10. These can potentially expose the solid substrate to the plasma and cause surface degradation. Moreover, an inclined LM surface may be differentially heated by the impinging plasma, accelerating evaporation or reducing its ability to protect the underlying substrate.

The performance of a liquid-lithium system with an electrically-conductive substrate was also evaluated. The material of the substrate was tungsten, as it is desirable for fusion applications. Results from simulations are shown in

figure 14. Overall, there is no significant difference between the flows obtained with different injected currents $I_0 = 0$ A and $I_0 = 50$ A, as most of the externally applied current is carried through the substrate and not through the LM ($\sigma_W = 16 \text{ MS m}^{-1}$, $\sigma_{Li} = 3.43 \text{ MS m}^{-1}$). Flow propulsion with external currents is not achievable for lithium flows with substrates made of materials more electrically conductive than the LM itself. Moreover, electrically conductive boundaries enhance MHD drag in LM flows [38], decelerating the flow even further.

3.3. Reactor-scale operation

3.3.1. Power requirements for the implementation of $\mathbf{j} \times \mathbf{B}$ -thrust. A LM-divertor system could be designed such that the flow follows the field lines, hence minimizing the magnitude of the surface-normal field \mathbf{B}_n . However, this

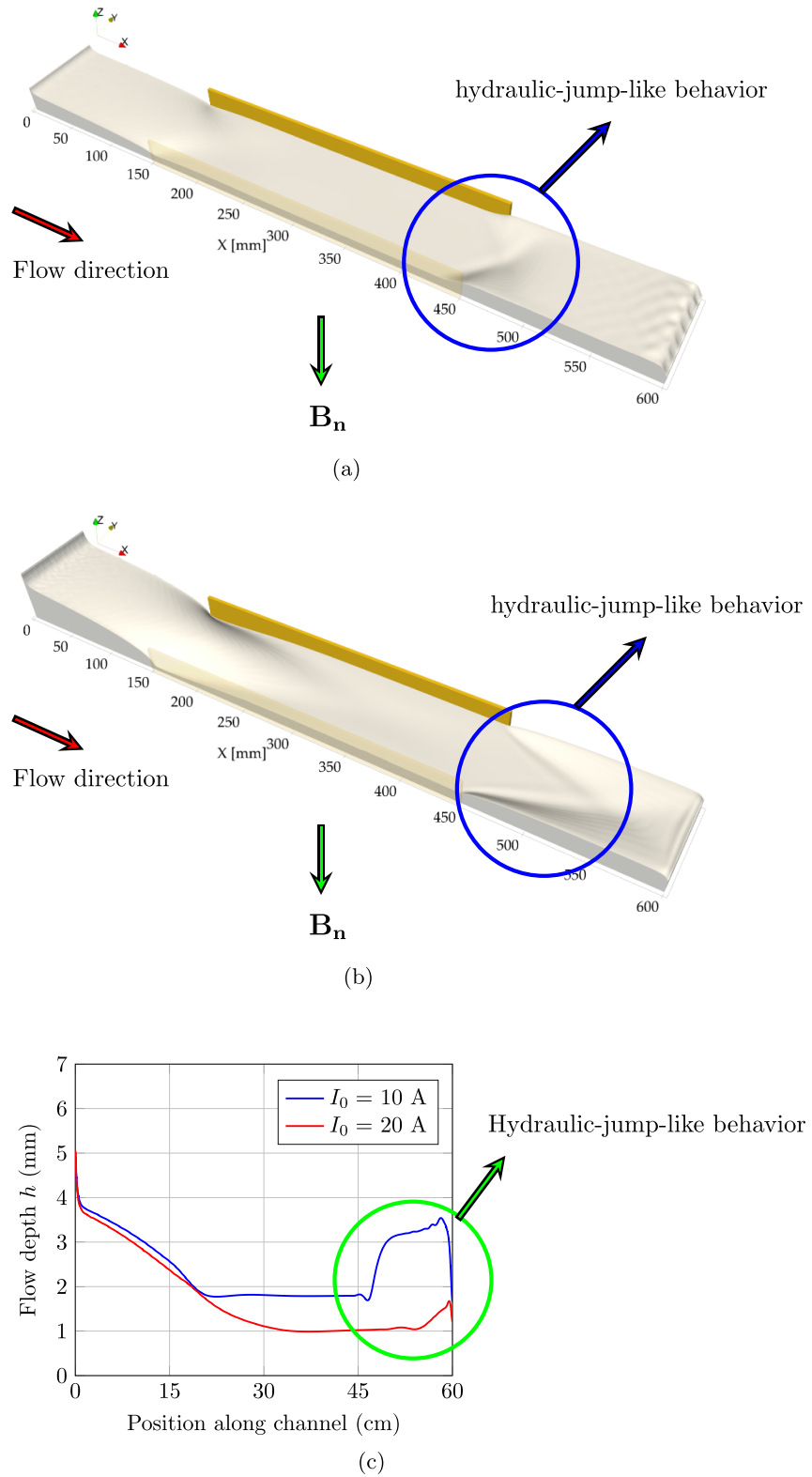


Figure 11. Simulation results for flow with insulated substrate, $|\mathbf{B}_n| = 0.103 \text{ T}$ and $Q = 1.9 \text{ L min}^{-1}$. (a) Simulation result for $I_0 = 10 \text{ A}$. h is augmented by a factor of 5. (b) Simulation result for $I_0 = 20 \text{ A}$. h is augmented by a factor of 10. (c) h -profiles.

implies that higher currents would be required to apply $\mathbf{j}_e \times \mathbf{B}_n$ -thrust. Moreover, MHD drag from the toroidal field \mathbf{B}_T of a fusion device is unavoidable if chutes are installed in the divertor-cassette configuration. For operation

at the reactor scale, $\mathbf{j} \times \mathbf{B}$ -thrust could be aimed to be of the same order of magnitude as the expected MHD-drag forces from the total magnetic field $\mathbf{B} = \mathbf{B}_T + \mathbf{B}_n$ fields, meaning $|\mathbf{j}_e \times \mathbf{B}_n| \approx |\sigma(\mathbf{E} + \mathbf{U} \times \mathbf{B}) \times \mathbf{B}|$, where \mathbf{U} is the

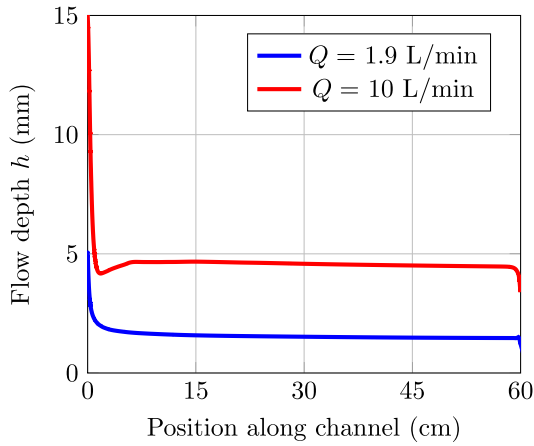


Figure 12. h -profiles with $\mathbf{j} \times \mathbf{B}$ -thrust ($I_0 = 20$ A, $|\mathbf{B}_n| = 0.103$ T) from simulation at different flow rates and non-conductive substrate.

velocity field and \mathbf{E} is the electric field of the LM flow, respectively .

The term $|\sigma(\mathbf{E} + \mathbf{U} \times \mathbf{B}) \times \mathbf{B}|$ could be approximated as $\sim \sigma C_M |\mathbf{U}| |\mathbf{B}|^2$ [38], where C_M is a coefficient that takes into account the dependence of the MHD drag force on the electrical conductivity and thickness of the walls around the LM flow. This estimate has been used previously to simplify the analysis free surface flows [11, 39]. $|\mathbf{U}|$ is approximated as $|\mathbf{U}| \sim v_{cr}$ (see equation (2)), which is a rough estimate of the flow speed required to avoid evaporation of the LM [3]. Finally, after evaluating $|\mathbf{B}_T| \gg |\mathbf{B}_n|$, a rough approximation of the required applied current density is shown in equation (5)

$$|\mathbf{j}_e| \sim \sigma C_M \frac{4\alpha L}{\pi k \rho c} \left(\frac{q_{\perp}}{\Delta T_{cr}} \right)^2 \frac{|\mathbf{B}_T|^2}{|\mathbf{B}_n|}. \quad (5)$$

The calculation of the total electric current required to operate a LM system on the inner divertor target at the reactor scale is made with equation (5). $L = 5$ mm was chosen for the heat-flux width in these calculations. For an ITER-reactor scale, the total current I applied in a divertor target is estimated as $I \sim |\mathbf{j}_e| h L_0$, with $L_0 \sim 1$ m being the length of the divertor target split into cassettes [18], and a thickness $h \sim 1$ cm for the LM flow. The range $C_M < 0.1$ is characteristic of LM flows with insulated substrates based on approximations from [40].

Total power P is calculated as $P = I_{e,i}^2 R_{e,i} + I_{e,o}^2 R_{e,o}$, where $R_{e,i}$, $R_{e,o}$ are the electrical resistances of the LM flow on the inboard and outboard divertor targets. $I_{e,i}$, $I_{e,o}$ are the total currents applied on the inner and outer divertor targets, respectively. The total resistance of each target could be simplified assuming a single and continuous LM slab, thus $R_{e,i} = \frac{2\pi(R_0 - \frac{1}{2}L_0)}{\sigma h L_0}$ and $R_{e,o} = \frac{2\pi(R_0 + \frac{1}{2}L_0)}{\sigma h L_0}$, with R_0 as the major radius of the reactor. Both inboard and outboard targets are assumed to be of the same length L_0 . Finally, power requirements for the inner divertor target are shown in figure 15.

Figures 15(a) and (b) show the toroidal and poloidal field distribution on the cross section of ITER. These were used as reference for calculations of power requirements. The neighborhood of the divertor regions has $|\mathbf{B}_T| \sim 10$ T for the

inboard target, and $|\mathbf{B}_T| \sim 6$ T for the outboard target. $|\mathbf{B}_n| \sim 0.1$ T or less for both targets.

From figures 15(c) and (d), it is noticeable that the power required for operation of a fast-flow LM divertor is excessive. Compared to the 500 MW power output expected from a fusion device like DEMO [41], the inner LM-divertor target could require at least 20% of this power output (see figure 15(c)), which does not even include the power requirements to pump the LM into the reactor.

Furthermore, figure 15(d) shows how the inboard LM-divertor target could exceed the total power output expected by DEMO if $|\mathbf{B}_n| \ll 0.1$ T, which could be expected according to figure 15(b). As a note, previous reports suggest that LM systems for heat exhaust in divertors should aim to require less than 5% of the total power output expected from a fusion device [10], primarily for economic viability, and this proposed approach is far from reaching this goal.

As a reminder to the reader, a coefficient of $C_M < 0.1$ was used for this calculation, which would imply the construction of electrically insulated substrates for the LM flow. Electrically conductive materials in contact with the LM flows, such as tungsten with wall thickness of a few millimeters, would yield $C_M > 0.1$. The latter would greatly increase power requirements for the operation of these systems. Additionally, if the flow cassettes are made of materials with higher electrical conductivity to that of the LM flow, they would take a portion (if not all) of the injected electrical current to generate $\mathbf{j} \times \mathbf{B}$ -thrust in the LM flow. The latter would completely ruin the method proposed in this article for countering MHD drag.

Furthermore, the previous calculations were made for $10 \text{ MW m}^{-2} < q_{\perp} < 31 \text{ MW m}^{-2}$, which corresponds to predictions for ITER [1]. However, heat loads will be more demanding in future commercial fusion reactors. Thus, power requirements are expected to increase [42] as faster flows would be needed to avoid overheating of LMs. If higher flow speeds during operation are desired, not only power requirements would increase, but attempting to thrust a flow with $\mathbf{j} \times \mathbf{B}$ -thrust could generate the same instabilities described in section 3.2.

3.3.2. Instabilities from reactor plasmas. Further problematics for a LM-flow system could be mentioned, mainly concerning the angle of incidence of the heat-flux load. For instance, the angle of incidence between the free surface of the LM flow at the divertor targets and the magnetic field \mathbf{B} of ITER should be at most 3° (4.5° if the toroidal bevel is included) to avoid excessive heat deposition on the system from q_{\parallel} . However, any ripple at the free surface of the LM flow at the divertor would significantly increase the angle of incidence, which would lead to intense overheating of the LM and subsequent evaporation.

Following the discussion on the issues caused by ripples that free surface of the LM flow in the divertor, one should consider that the plasma above the LM flow in the divertor would create a velocity shear at the free-surface and cause Kelvin–Helmholtz instabilities [43]. This would either

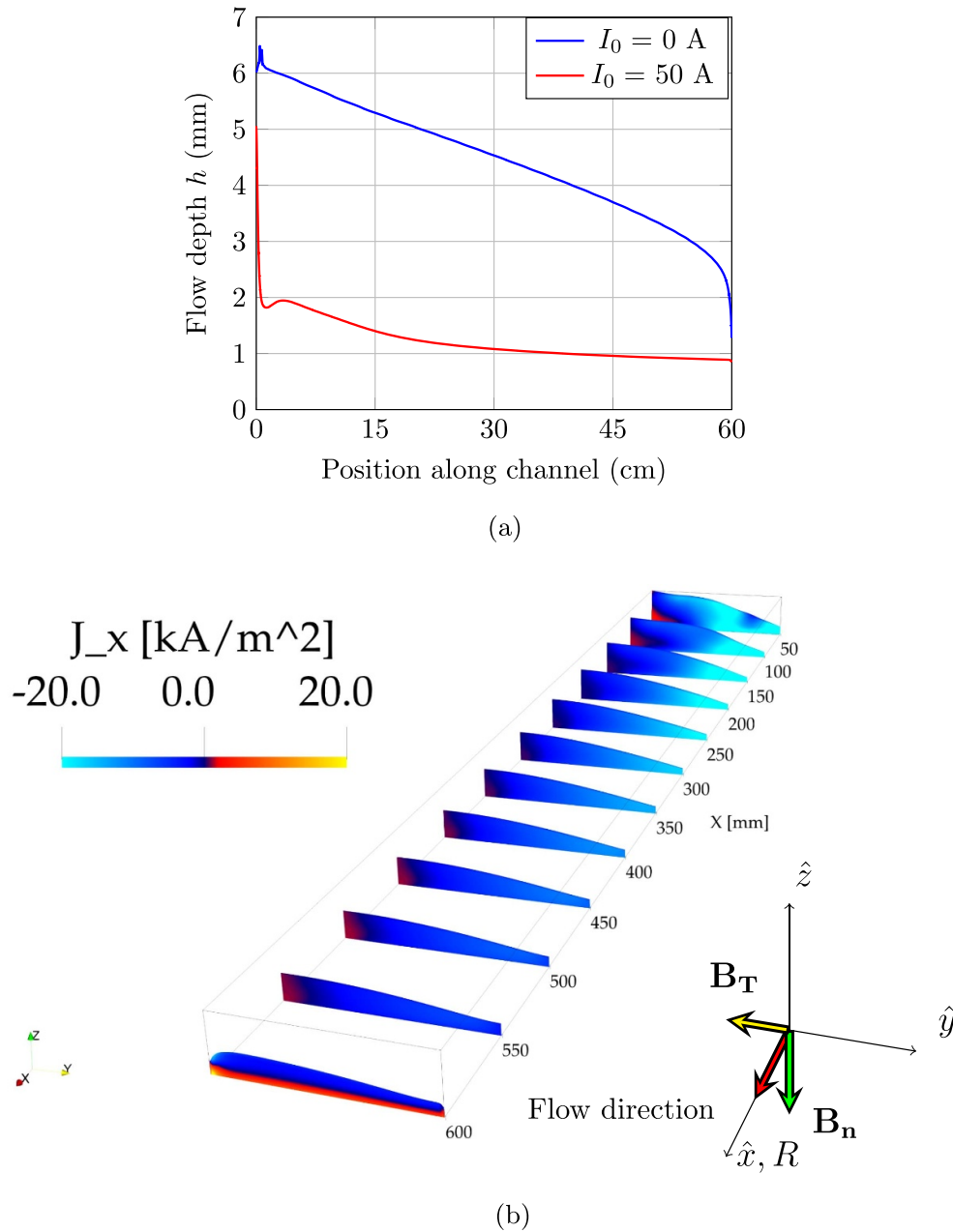


Figure 13. Simulation results for lithium flow with insulated substrate, $|\mathbf{B}_T| = 1 \text{ T}$ and $|\mathbf{B}_n| = 0.1 \text{ T}$, $Q = 2 \text{ L min}^{-1}$. (a) h -profiles with insulating substrate at different external currents I_0 . Note: the profiles shown correspond to the plane at the center of the width of the channel. (b) Stream-wise currents for $I_0 = 50 \text{ A}$. h is increased by a factor of 10.

create waves on the LM free surface or enhance the amplitude of the existing ones. Overall, the angle of incidence is not expected to be easily controlled on these type of flows.

In spite of this, LM evaporation is not desired as it would introduce impurities into the plasma core. However, it could be acceptable for liquid lithium as it would operate with the vapor shielding mechanism, which has been proven to be beneficial to avoid overheating on PFCs exposed to heat loads [44]. Nevertheless, leaving liquid lithium as the only alternative for a LM-divertor system already constrains the design options.

3.3.3. Alternatives for LM-flow divertors. Even though this paper presents a pessimistic revision of the $\mathbf{j} \times \mathbf{B}$ -thrust approach, there is room for improvements for chute flows in divertors. The main problematic is the source of MHD drag for divertor LM flows, which is proportional to \mathbf{B}_T , while the source of $\mathbf{j} \times \mathbf{B}$ -thrust is proportional to $\mathbf{B}_n \sim \mathbf{B}_p$. One could take advantage of externally injected currents that are parallel (or anti-parallel, depending on the direction of the flow) to \mathbf{B}_n . The latter would generate a source of thrust that is proportional the toroidal magnetic field \mathbf{B}_T , which would yield much faster flow with smaller power requirements compared to those in figure 15. The method to apply these currents in

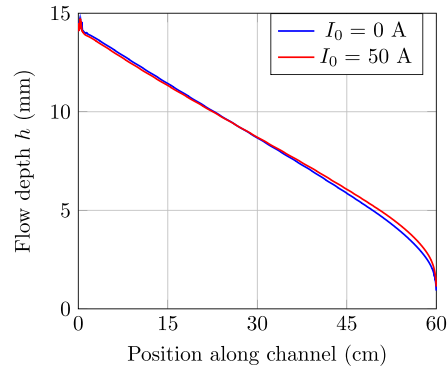


Figure 14. Simulation results with a tungsten substrate with $t_w = 1/8$ in, $|\mathbf{B}_T| = 1$ T and $|\mathbf{B}_n| = 0.1$ T, $Q = 2$ L min $^{-1}$. (a) h -profiles for different external currents.

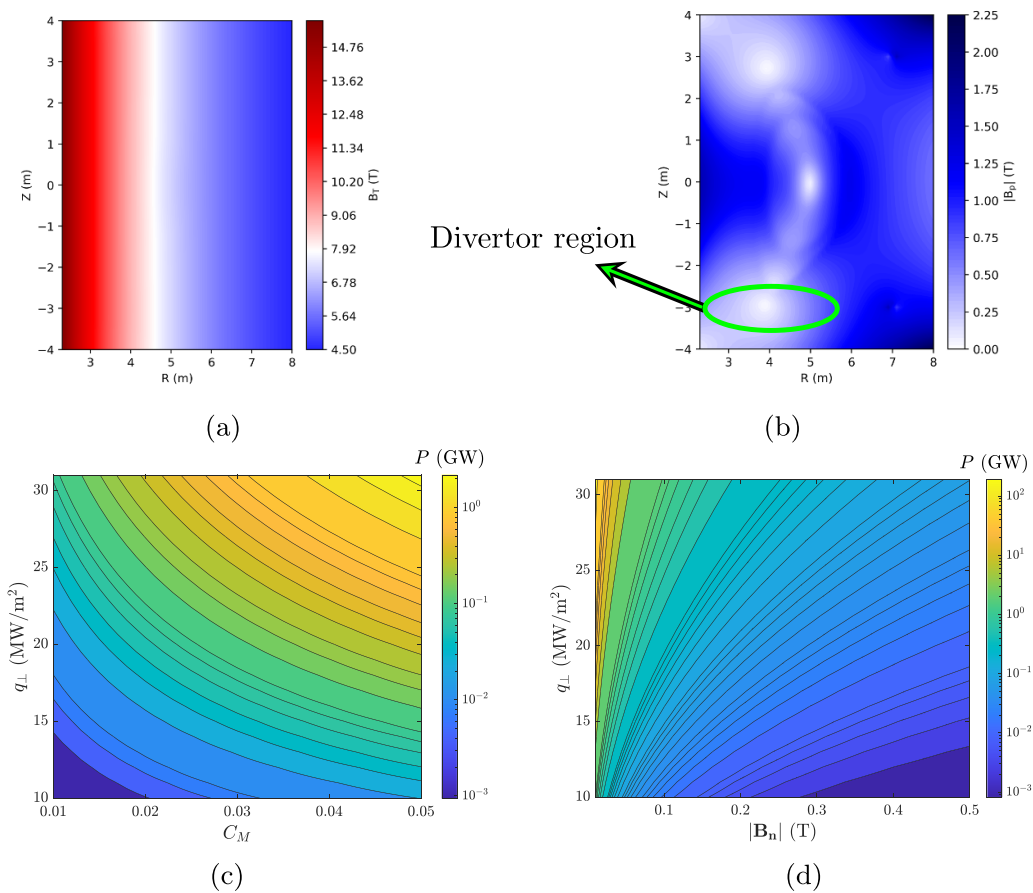


Figure 15. Projections at the reactor scale for a LM divertor with $\mathbf{j} \times \mathbf{B}$ -thrust. (a) Toroidal field \mathbf{B}_T of ITER. (b) Poloidal field \mathbf{B}_P of ITER. (c) Power requirements for both inboard and outboard LM-divertor targets with $\mathbf{j} \times \mathbf{B}$ -thrust. Note: $|\mathbf{B}_T| = 10$ T, $|\mathbf{B}_n| = 0.1$ T for the inboard divertor, $|\mathbf{B}_T| = 6$ T, $|\mathbf{B}_n| = 0.1$ T for the outboard divertor. (d) Power requirements for an inboard LM-divertor target with $\mathbf{j} \times \mathbf{B}$ -thrust. Note: $|\mathbf{B}_T| = 10$ T, $C_M = 0.05$.

said flows, and the analysis on intrinsic challenges, are left for future work.

It is worth mentioning alternate concepts that do not encounter the concerns emphasized previously. Certainly, operating in the ‘slow flow’ range (below 1 m s $^{-1}$) is useful to guarantee stable free-surface flows with nearly negligible surface ripples and waves, and reduced ejection of LM droplets into the reactor plasma. Previous reports on the

capillary porous systems [45–47], the lithium metal infused trenches (LiMIT) [48], FLiLi [49] and divertorlets [10, 11] describe how these configurations attempt to handle high heat loads while generating ‘nearly flat’ flow surfaces. In particular, the LiMIT and divertorlets concepts have a ‘pumping force’ that is proportional to the toroidal magnetic field, which allows them to operate with small power requirements compared to those in figure 15.

4. Conclusions

This work presented the results of experiments of FSLMFs subject to different conditions. Experimental results were analyzed with a reformulation of the SFSFM. Similar trends were found between experiment data and calculations from the simplified momentum equation from the SFSFM. Moreover, three-dimensional effects of electric currents were analyzed with FreeMHD simulations. The same trends of the SFSFM and experiments were obtained, which validated the applicability of FreeMHD to simulate these scenarios.

$\mathbf{j} \times \mathbf{B}$ -thrust was not proven experimentally since the outlet of the LMFREX channel caused LM accumulation. However, FreeMHD simulations were used to analyze the effect of an outlet condition that eliminates LM accumulation in the channel. These simulations showed that $\mathbf{j} \times \mathbf{B}$ -thrust is capable of accelerating the flow, but could yield flow detachment from the side walls of the channel due to fringing currents, which would imply an exposed solid substrate to heat loads from fusion plasmas.

Additionally, FreeMHD simulations were also performed to study the effect of insulated and conductive substrates on LM-fast-flow divertors. Insulated substrates allowed the flow to accelerate while pushing the flow to one side wall of the chute, which is not desirable for reactor operation. In the case of a conductive substrate, a tungsten chute not only ruined the application of external currents in the LM flow, but also enhanced MHD drag, which did not allow achieving flow propulsion.

With regard to power requirements for LM-fast-flow divertors with electrically insulated substrates, these systems are inefficient if thrust is expected by means of the surface-normal field \mathbf{B}_n . Furthermore, electrically conductive substrates are more inefficient, since they carry a portion of the injected current for Lorentz-force propulsion and also enhance MHD drag forces on the LM flows.

Countering MHD drag forces in LM-divertors with $\mathbf{j} \times \mathbf{B}$ -thrust is far from being commercially attractive for fusion reactors. Furthermore, the main function of LM systems in fusion reactors is to avoid direct contact of fusion plasmas with solid components, a function that has been shown to be put at risk when applying $\mathbf{j} \times \mathbf{B}$ -thrust.

This paper showed that the $\mathbf{j} \times \mathbf{B}$ -thrust approach is intrinsically unstable, even without the instabilities in LM flows already known to be caused by reactor plasmas. Future work for this method may involve the application of currents to generate thrust with the toroidal magnetic field inside a reactor. Moreover, further research may be focused on slow-speed LM concepts that do not encounter all the problems inherent to the $\mathbf{j} \times \mathbf{B}$ -thrust approach.

Acknowledgments

The research described in this paper was conducted under the Laboratory Directed Research and Development (LDRD)

Program at Princeton Plasma Physics Laboratory, a national laboratory operated by Princeton University for the U.S. Department of Energy under Prime Contract No. DE-AC02-09CH11466.

This manuscript is based upon work supported by the U.S. Department of Energy, Office of Science, Office of Fusion Energy Sciences, and has been authored by Princeton University under Contract No. DE-AC02-09CH11466 with the U.S. Department of Energy.

This research was also supported by the Natural Science Foundation of Zhejiang Province, China (No. LQ21E090011). The work presented in this article would not be possible without the support of the Oroshhi-2 Team at the National Institute for Fusion Science, Kyoto University and the Research Institute for Applied Mechanics of Kyushu University.

The publisher, by accepting the article for publication, acknowledges that the United States Government retains a non-exclusive, paid-up, irrevocable, worldwide license to publish or reproduce the published form of this manuscript, or allow others to do so, for United States Government purposes.

Appendix A. Shallow free-surface flow model with Lorentz forces

A.1. Navier Stokes equations

Consider a steady-state flow field with two components: $\mathbf{U} = (u, 0, w)$, u being the longitudinal component (stream-wise direction, x -direction), and w being the vertical component (in the z -direction). Incompressible flow with mass continuity is assumed: $\nabla \cdot \mathbf{U} = 0$. All forces are assumed to be applied in the stream-wise direction, parallel to the u -component. The governing equations are as follows:

$$\left. \begin{aligned} \frac{\partial u}{\partial x} + \frac{\partial w}{\partial z} &= 0 \\ \rho(\mathbf{U} \cdot \nabla)u &= -\frac{\partial p}{\partial x} + (\mathbf{j} \times \mathbf{B})_x + \mu \nabla^2 u \end{aligned} \right\}. \quad (6)$$

SFSFM proposes the separation of variables for $u = vf$, where v is the local average flow speed $v = \int_0^h u dz$ and $f(\eta, \lambda) = a\eta + b\eta^2 + c\eta^3$; $\eta = z/h$. h is the local flow depth and λ is a parameter that evaluates the stream-wise variation of the velocity profile. The inclusion of f allows the evaluation of viscous forces for this 1D model [32].

The parameter a is set to be $a = \lambda + 3$ as done previously in literature. The parameter λ determines where a flow separation or a discontinuity could occur, and the choice of $a = \lambda + 3$ has no effect on the flow behavior, it simply changes the value of λ where a discontinuity occurs. The parameters b and c are found with mass continuity: $\int_0^1 f d\eta = 1$, and zero-stress at the free boundary: $\frac{\partial f}{\partial \eta} \Big|_{\eta=1} = 0$ [36]. The final solution of f is shown in

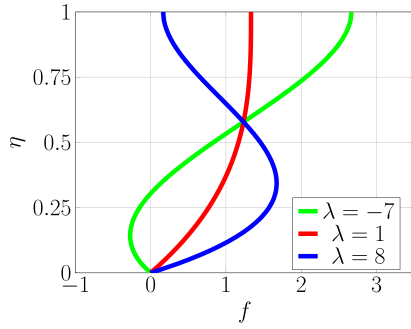


Figure 16. Velocity profile variation along y and z directions.

equation (7). The shape of f for different values of λ is shown in figure 16

$$f(\eta, \lambda) = (3 + \lambda)\eta + \frac{1}{2}(5\lambda + 3)\eta^2 - \frac{4}{3}\lambda\eta^3. \quad (7)$$

A.2. Hydrostatic pressure

The pressure field is assumed to be hydrostatic: $p = p_a + \rho g(h - z)$. p_a is the pressure generated by the gas on top of the LM flow. If p_a is assumed to be invariant during experiments, then $\frac{\partial p}{\partial x} = \rho g \frac{\partial h}{\partial x}$.

A.3. Lorentz forces

Furthermore, the electric currents in the LM could be considered as a superposition of an external current density \mathbf{j}_e (the one that is injected with the electrodes), and the MHD-induced current $\mathbf{j}_i = (\mathbf{E} + \mathbf{U} \times \mathbf{B})$. \mathbf{j}_e depends on the total current injected in the LM and the consequent flow-depth profile.

Figure 17(a) shows the setup for current injection used for calculations in COMSOL (finite element simulation solver): 15 wires connected at a single joint on each side, carrying the current to the rectangular electrodes, simulating a configuration similar to that of the experiments executed.

Figure 17(b) shows the variation of the flow-depth-average current density profile. Calculations of current density profiles were performed with the Electric Currents module in COMSOL [50], including the geometry of the LMFREX channel and the copper electrodes.

For figure 17(b), a generic flow-depth profile was used for the calculation of \mathbf{j}_e . It is observable that a variation of h along the channel has an impact on the current density profile. The simplification $\mathbf{j}_e \approx j_e \hat{x}$ is applied since vertical variations (z -direction) of the current density \mathbf{j}_e are negligible. However, it must be noted that there is a fringing effect for the conduction of the injected current. Given that the injected current satisfies $\nabla \cdot \mathbf{j}_e$, other components for the current density are expected near the edges of the electrodes, causing different Lorentz forces in the LM flow. This is further discussed in section 3.2.

For calculations of current density profiles, a flow-depth profile was initially assumed and imported to COMSOL [50]. The corresponding \mathbf{j}_e -distribution would be calculated

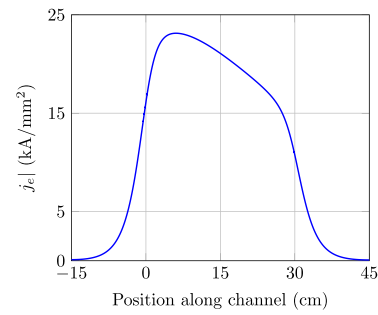
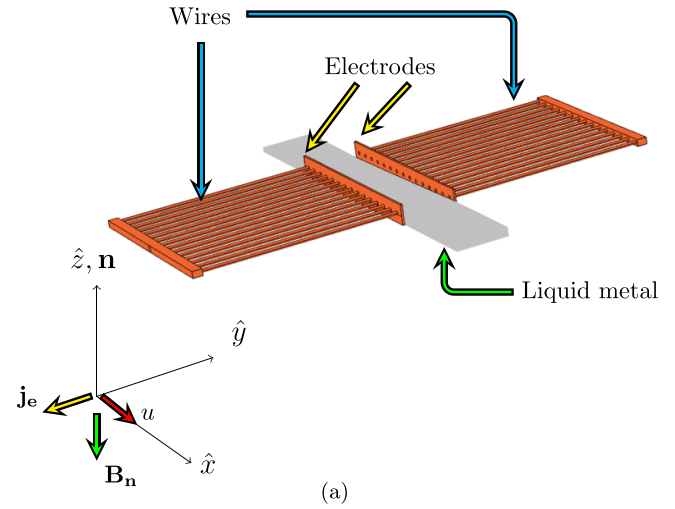


Figure 17. Diagram of simulation setup and current density j_e for a given h -profile in a galinstan flow. $I_0 = 60$ A. (a) Wires for current injection, electrodes and LM slab. (b) Height-average current density j_e .

accordingly and used in the SFSFM to find the resulting flow depth profile. This procedure was repeated until reaching an agreement between resulting flow profiles and respective current density distributions.

MHD drag force on a free-surface flow is approximated as a fictitious pressure drop [40]. The formulas are derived for closed-pipe-fully-developed flows, but their applicability has been shown previously for free-surface flows with small Hartmann numbers [39].

$$\sigma(\mathbf{j}_i \times \mathbf{B})_x \propto - \left(\frac{\partial p}{\partial x} \right)_{\text{MHD drag}} = - \frac{\mu v}{(h/2)^2} P_H \quad (8)$$

$$P_H = \frac{Ha^2 \tanh Ha}{Ha - \tanh Ha} - 3 \quad Ha = |\mathbf{B}_n| \left(\frac{h}{2} \right) \sqrt{\frac{\sigma}{\mu}}$$

A.4. Viscous forces

Viscous forces were simplified as $\mu \nabla^2 u \approx \mu \frac{\partial^2 u}{\partial z^2}$, as $\left| \frac{\partial^2 u}{\partial z^2} \right| \gg \left| \frac{\partial^2 u}{\partial x^2} \right|, \left| \frac{\partial^2 u}{\partial y^2} \right|$, based on dimensional analysis [36]. Moreover, free-surface-thin-film flows encounter turbulent fluctuations

that enhances the eddy viscosity. As previously reported with experimental results, the magnitude of flow depth in free surface channel flows is not consistent with results from models that only include laminar viscous drag [32].

For the analysis of jump discontinuity-like experiments exclusively, the viscosity was modeled as $\mu \rightarrow \rho(\nu_L + \nu_\tau)$ [31–33], where ν_L is the kinematic fluid viscosity and ν_τ is the kinematic eddy viscosity. ν_τ is modeled with a mixing length l_m , according to Prandtl's mixing-length theory [28, 51–53].

Since flow depths h during experiments were smaller than the flow width W , the expression of the eddy viscosity could be further simplified as $\nu_\tau = l_m^2 \left| \frac{\partial u}{\partial z} \right|$. The magnitude of the mixing length varies across the flow depth [51, 54]. For this reason, an average magnitude for the kinematic eddy viscosity is considered to further simplify the model, thus $\nu_\tau \approx k^2 q$, with $k = 0.05$ (k should not be confused with the Von Kármán constant). In general, the SFSFM is sensitive to initial conditions, so k was used to find a solution that is continuous for all variables in the x -domain (a discontinuity is caused when $\lambda = 7/2$ or $h = 0$ [36]).

A.5. Governing equations

Substituting all the previous simplifications for the body forces in equation (6) and dividing both sides by ρ , equation (9) is obtained. After substituting the equation for mass continuity in the momentum equation, and height-averaging both sides, equation (10) is obtained. G is defined as $G(\lambda) = \int_0^1 f^2 d\eta$, and $q = QW^{-1}$, $v = qh^{-1}$, where Q is the volumetric flow rate

$$\frac{\partial u}{\partial x} + \frac{\partial w}{\partial z} = 0$$

$$u \frac{\partial u}{\partial x} + w \frac{\partial u}{\partial z} = -g \frac{\partial h}{\partial x} + \frac{j_e B}{\rho} - 4\nu_L h^{-2} v P_H + (\nu_L + \nu_\tau) \frac{\partial^2 u}{\partial z^2} \quad (9)$$

$$\underbrace{v \frac{\partial(Gv)}{\partial x}}_{(\mathbf{U} \cdot \nabla)u} = \underbrace{-g \frac{\partial h}{\partial x}}_{\nabla p / \rho} + \underbrace{\frac{j_e B}{\rho}}_{\mathbf{j}_e \times \mathbf{B} / \rho} + \underbrace{-4\nu_L h^{-2} v P_H}_{\mathbf{j}_i \times \mathbf{B} / \rho} + \underbrace{(\nu_L + k^2 q) h^{-2} v \left(\frac{\partial f}{\partial \eta} \right) \Big|_{\eta=0}}_{\nu \frac{\partial^2 u}{\partial z^2}}. \quad (10)$$

Equation (10) has two dependent variables v and λ , thus two governing equations are required. The governing equation for λ is derived by expanding the $v \frac{\partial(Gv)}{\partial x}$ term as $v \frac{\partial(Gv)}{\partial x} = v^2 \frac{\partial G}{\partial \lambda} \frac{\partial \lambda}{\partial x} + \frac{1}{2} G \frac{\partial(v^2)}{\partial x}$, which is shown in equation (11).

$$\frac{\partial \lambda}{\partial x} = \frac{1}{v^2 \frac{\partial G}{\partial \lambda}} \left[-\frac{1}{2} G(\lambda, \eta) \partial_x v^2 - g \frac{\partial h}{\partial x} + \frac{j_e B}{\rho} + -4\nu_L h^{-2} v P_H + \dots + (\nu_L + k^2 q) h^{-2} v \left(\frac{\partial f}{\partial \eta} \right) \Big|_{\eta=0} \right]. \quad (11)$$

The governing equation for h is obtained by evaluating equation (9) at $z=0$. Due to the no-slip condition at $z=0$, $(\mathbf{U} \cdot \nabla)u = 0$ and a solution for $\frac{\partial h}{\partial x}$ is found. Since this model is not solving for the 3D-MHD-induced currents that are induced in the LM, the term $(\mathbf{j} \times \mathbf{B})_x$ could be simplified by just considering the externally applied current \mathbf{j}_e . The evolution of h is then dictated by equation (12). Solutions for equations (11) and (12) were computed using a 4th-order Runge–Kutta scheme

$$\frac{\partial h}{\partial x} = g^{-1} \left\{ \frac{j_e B}{\rho} + q h^{-3} (\nu_L + k^2 q) \left(\frac{\partial^2 f}{\partial \eta^2} \right) \Big|_{z=0} \right\}. \quad (12)$$

Appendix B. Governing equations and boundary conditions on FreeMHD

Assuming an incompressible two-phase flow, the continuity and momentum equations read:

$$\nabla \cdot \mathbf{U} = 0 \quad (13)$$

$$\frac{\partial \rho \mathbf{U}}{\partial t} + \nabla \cdot (\rho \mathbf{U} \otimes \mathbf{U}) = -\nabla p + \nabla \cdot [\mu (\nabla \mathbf{U} + \nabla \mathbf{U}^T)] + \mathbf{J} \times \mathbf{B} + \mathbf{F}_{st}, \quad (14)$$

where \otimes represents the tensor product, μ is the dynamic viscosity and \mathbf{F}_{st} is the surface tension force. The immiscible liquid and gas phases are modeled using the volume of fluid method, where the volume fraction, $\alpha_i \in [0, 1]$, is used to indicate the fraction of a computational cell that is occupied by the liquid. The interface between the liquid and gas is the iso-surface of $\alpha = 0.5$, which is captured using the MULES scheme [55]. A physical property of the fluid mixture in a computational cell, ψ_i , such as density, viscosity, or electrical conductivity is consequently computed using $\psi_i = \psi_l \alpha_i + (1 - \alpha_i) \psi_g$ where ψ_l and ψ_g are the values for the liquid and gas phases, respectively. The surface tension force is calculated using the continuum surface force model, such that:

$$\mathbf{F}_{st} = \sigma_{st} \nabla \cdot \left[\frac{\nabla \alpha_i}{|\nabla \alpha_i|} \right] \nabla \alpha_i, \quad (15)$$

where σ_{st} is the surface tension coefficient.

Since the magnetic Reynolds number $R_m \sim \sigma \mu_0 U W \ll 1$ for all flows studied in this work, the induced magnetic field is negligible and the electrical field can be described in terms

of the electric scalar potential ϕ . The electric current density is thus computed with equation (16)

$$\mathbf{J} = \sigma(-\nabla\phi + \mathbf{U} \times \mathbf{B}). \quad (16)$$

Using charge conservation, $\nabla \cdot \mathbf{J}$, and equation (16) the electric scalar potential is computed by solving the following Poisson equation:

$$\nabla \cdot (\sigma \nabla \phi) = \nabla \cdot (\sigma \mathbf{U} \times \mathbf{B}). \quad (17)$$

To account for the effect of electrically conductive boundaries, a conjugate solution strategy is employed where equation (17) is solved both in the fluid and solid regions of the domain. Using charge conservation and the no-slip condition for velocity, the boundary condition for ϕ at the fluid–solid interface is derived by enforcing the continuity of the boundary-normal electric current density:

$$[\mathbf{J} \cdot \mathbf{n}]_f = [\mathbf{J} \cdot \mathbf{n}]_s \quad (18)$$

where \cdot_f and \cdot_s denote the fluid and solid sides of the interface, respectively. Consequently, the boundary condition on ϕ reads as follows:

$$\left[\sigma \frac{\partial \phi}{\partial \mathbf{n}} \right]_f = \left[\sigma \frac{\partial \phi}{\partial \mathbf{n}} \right]_s, \quad (19)$$

which reduces to the homogeneous Neumann boundary condition at electrically insulating boundaries. At boundaries through which an external electric current is injected, the boundary condition simply reads

$$\frac{\partial \phi}{\partial \mathbf{n}} = \frac{I_0}{\sigma A} \quad (20)$$

where I_0 is the externally applied current, A is the surface area of the boundary and σ is the electrical conductivity of the LM. Assuming no electric current can enter or exit the domain through inlets and outlets, their boundary condition for the electric scalar potential is in equation (21):

$$\frac{\partial \phi}{\partial \mathbf{n}} = (\sigma \mathbf{U} \times \mathbf{B}) \cdot \mathbf{n}. \quad (21)$$

ORCID iDs

F. Saenz  <https://orcid.org/0000-0001-7456-590X>
 A.E. Fisher  <https://orcid.org/0000-0003-1744-6984>
 B. Wynne  <https://orcid.org/0000-0002-0593-2195>
 Z. Sun  <https://orcid.org/0000-0002-7224-3592>
 E. Kolemen  <https://orcid.org/0000-0003-4212-3247>

References

- [1] Horacek J. et al 2021 Predictive modelling of liquid metal divertor: from compass tokamak towards upgrade *Phys. Scr.* **96** 124013
- [2] Pitts R. et al 2019 Physics basis for the first ITER tungsten divertor *Nucl. Mater. Energy* **20** 100696
- [3] Jaworski M., Brooks A., Kaita R., Lopes-Cardozo N., Menard J., Ono M., Rindt P. and Tresemer K. 2016 Upgrades toward high-heat flux, liquid lithium plasma-facing components in the NSTX-U *Fusion Eng. Des.* **112** 93–101
- [4] Majeski R. 2009 Plasma interaction in controlled fusion devices *AIP Conf. Proc.* **1237** 122–37
- [5] Wischmeier M. 2015 High density operation for reactor-relevant power exhaust *J. Nucl. Mater.* **463** 22–29
- [6] Smolentsev S. 2021 Design window for open-surface lithium divertor with helium-cooled substrate *Fusion Eng. Des.* **173** 112930
- [7] Kolemen E., Hvasta M., Majeski R., Maingi R., Brooks A. and Kozub T. 2019 Design of the flowing liquid torus (FLIT) *Nucl. Mater. Energy* **19** 524–30
- [8] Shimada M. and Hirooka Y. 2014 Actively convected liquid metal divertor *Nucl. Fusion* **54** 122002
- [9] Zakharov L.E. 2003 Magnetic propulsion of intense lithium streams in a tokamak magnetic field *Phys. Rev. Lett.* **90** 045001
- [10] Fisher A., Sun Z. and Kolemen E. 2020 Liquid metal “divertorlets” concept for fusion reactors *Nucl. Mater. Energy* **25** 100855
- [11] Saenz F., Sun Z., Fisher A., Wynne B. and Kolemen E. 2022 Divertorlets concept for low-recycling fusion reactor divertor: experimental, analytical and numerical verification *Nucl. Fusion* **62** 086008
- [12] Incropera F. 2006 *Fundamentals of Heat and Mass Transfer* 6th edn (Wiley)
- [13] Horacek J. et al 2020 Scaling of L-mode heat flux for ITER and COMPASS-U divertors, based on five tokamaks *Nucl. Fusion* **60** 066016
- [14] Chang C., Ku S., Hager R., Churchill R., Hughes J., Köchl F., Loarte A., Parail V. and Pitts R. 2021 Constructing a new predictive scaling formula for ITER’s divertor heat-load width informed by a simulation-anchored machine learning *Phys. Plasmas* **28** 022501
- [15] Davison H.W. 1968 *Compilation of Thermophysical Properties of Liquid Lithium* vol 4650 (National Aeronautics and Space Administration)
- [16] Abdou M. et al 2001 On the exploration of innovative concepts for fusion chamber technology *Fusion Eng. Des.* **54** 181–247
- [17] Nygren R. et al 2004 A fusion reactor design with a liquid first wall and divertor *Fusion Eng. Des.* **72** 181–221
- [18] Fusion for Energy 2018 European prototypes for ITER divertor cassette completed (available at: <https://fusionforenergy.europa.eu/news/european-prototypes-for-iter-divertor-cassette-completed/#>) (Accessed 13 July 2022)
- [19] Al-Salami J., Saenz F., Wynne B., Sun Z., Hu C., Hanada K. and Kolemen E. 2023 FreeMHD (available at: <https://github.com/PlasmaControl/FreeMHD.git>)
- [20] Sun Z., Al-Salami J., Khodak A., Saenz F., Wynne B., Maingi R., Hanada K., Hu C. and Kolemen E. 2023 Magnetohydrodynamics in free surface liquid metal flow relevant to plasma facing components *Nucl. Fusion* **63** 076022
- [21] Muroga T., Fukada S. and Hayashi T. 2019 Overview of fusion engineering research in Japan focusing on activities in nifs and universities *Fusion Sci. Technol.* **75** 559–74
- [22] Kusumi K., Kunugi T., Yokomine T., Kawara Z., Wu Y., Sagara A. and Tanaka T. 2019 Thermal mixing enhancement of liquid metal film-flow by various obstacles under vertical magnetic field *Fusion Eng. Des.* **146** 2158–62
- [23] Sagara A., Tanaka T., Yagi J., Takahashi M., Miura K., Yokomine T., Fukada S. and Ishiyama S. 2015 First operation of the Flinak/LiPb twin loop Orosh2i-2 with a 3T SC magnet for R&D of liquid blanket for fusion reactor *Fusion Sci. Technol.* **68** 303–7

- [24] Tanaka T., Sagara A., Yagi J. and Muroga T. 2019 Liquid blanket collaboration platform Oroshi-2 at NIFS with FLiNaK/LiPb twin loops *Fusion Sci. Technol.* **75** 1002–9
- [25] Morley N.B., Smolentsev S. and Gao D. 2002 Modeling infinite/axisymmetric liquid metal magnetohydrodynamic free surface flows *Fusion Eng. Des.* **63–64** 343–51
- [26] Liu J. and Yi L. 2018 *Liquid Metal Biomaterials: Principles and Applications* (Springer Series in Biomaterials Science and Engineering) (Springer)
- [27] Fisher A.E., Kolemen E. and Hvasta M.G. 2018 Experimental demonstration of hydraulic jump control in liquid metal channel flow using Lorentz force *Phys. Fluids* **30** 067104
- [28] Schlichting H. and Gersten K. 2017 *Boundary-Layer Theory* (Springer)
- [29] Singha S.B., Bhattacharjee J.K. and Ray A.K. 2005 Hydraulic jump in one-dimensional flow *Eur. Phys. J. B* **48** 417–26
- [30] Liao C., Kazimi M.S. and LaBombard B. 1994 MHD effects on liquid metal film flow *Nucl. Eng. Des.* **146** 325–35
- [31] Bonn D., Andersen A. and Bohr T. 2009 Hydraulic jumps in a channel *J. Fluid Mech.* **618** 71–87
- [32] Dhar M., Das G. and Das P.K. 2020 Planar hydraulic jumps in thin film flow *J. Fluid Mech.* **884** A11
- [33] Dhar M., Das G. and Das P.K. 2021 Planar hydraulic jump and associated hysteresis in near horizontal confined flow *Phys. Rev. Fluids* **6** 084803
- [34] Dhar M., Ray S., Das G. and Das P.K. 2021 Internal hydraulic jump in plane poiseuille two-layer flow: theoretical, numerical and experimental study *J. Fluid Mech.* **912** A45
- [35] Dhar M., Ray S., Das G. and Das P.K. 2021 Modulation of viscous planar jump by an obstacle in the flow path—interrogation through shallow water equations and numerical analysis *Phys. Fluids* **33** 053609
- [36] Watanabe S., Putkaradze V. and Bohr T. 2003 Integral methods for shallow free-surface flows with separation *J. Fluid Mech.* **480** 233–65
- [37] Jasak H., Jemcov A. and Tukovic Z. 2007 OpenFOAM: a C++ library for complex physics simulations *Int. Workshop on Coupled Methods in Numerical Dynamics (Dubrovnik, Croatia, 19–21 September 2007)* vol 1000 (IUC Dubrovnik Croatia) pp 1–20 (available at: <https://csabai.web.elte.hu/http/simulationLab/jasakEtAlOpenFoam.pdf>)
- [38] Miyazaki K., Inoue S., Yamaoka N., Horiba T. and Yokomizo K. 1986 Magneto-hydro-dynamic pressure drop of lithium flow in rectangular ducts *Fusion Technol.* **10** 830–6
- [39] Hvasta M., Kolemen E., Fisher A. and Ji H. 2018 Demonstrating electromagnetic control of free-surface, liquid-metal flows relevant to fusion reactors *Nucl. Fusion* **58** 016022
- [40] Hoffman M.A. and Carlson G.A. 1971 Calculation techniques for estimating the pressure losses for conducting fluid flows in magnetic fields *Technical Report UCRL-51010* (California University, Lawrence Livermore National Laboratory)
- [41] EUROfusion 2022 The demonstration power plant: DEMO (available at: www.euro-fusion.org/programme/demo/) (Accessed 15 April 2022)
- [42] Zacha P. and Entler S. 2019 High heat flux limits of the fusion reactor water-cooled first wall *Nucl. Eng. Technol.* **51** 1251–60
- [43] Miloshevsky G. and Hassanein A. 2010 Modelling of Kelvin–Helmholtz instability and splashing of melt layers from plasma-facing components in tokamaks under plasma impact *Nucl. Fusion* **50** 115005
- [44] Van Eden G., Kvon V., Van De Sanden M. and Morgan T. 2017 Oscillatory vapour shielding of liquid metal walls in nuclear fusion devices *Nat. Commun.* **8** 192
- [45] Lyublinski I., Vertkov A., Mirnov S. and Lazarev V. 2015 Protection of tokamak plasma facing components by a capillary porous system with lithium *J. Nucl. Mater.* **463** 1156–9
- [46] Dejarnac R. et al 2020 Overview of power exhaust experiments in the compass divertor with liquid metals *Nucl. Mater. Energy* **25** 100801
- [47] Nygren R. and Tabarés F. 2016 Liquid surfaces for fusion plasma facing components—a critical review. Part I: physics and PSI *Nucl. Mater. Energy* **9** 6–21
- [48] Fiffis P., Morgan T., Brons S., Van Eden G., Van Den Berg M., Xu W., Curreli D. and Ruzic D. 2015 Performance of the lithium metal infused trenches in the magnum PSI linear plasma simulator *Nucl. Fusion* **55** 113004
- [49] Tang Z. et al 2020 Lithium splashing from flowing liquid lithium limiter and its effect on high confinement plasma performance in EAST tokamak *Nucl. Mater. Energy* **25** 100845
- [50] COMSOL 2020 *AC/DC Module User's Guide Version 5.6*
- [51] White F. 1991 *Viscous Fluid Flow (Mcgraw-Hill Series in Mechanical Engineering)* (McGraw-Hill)
- [52] Koçyigit M.B., Falconer R.A. and Lin B. 2002 Three-dimensional numerical modelling of free surface flows with non-hydrostatic pressure *Int. J. Numer. Methods Fluids* **40** 1145–62
- [53] Castro-Orgaz O. and Hager W. 2017 *Non-Hydrostatic Free Surface Flows (Advances in Geophysical and Environmental Mechanics and Mathematics)* (Springer International Publishing)
- [54] Cebeci T. 2013 General behavior of turbulent boundary layers *Analysis of Turbulent Flows With Computer Programs* 3rd edn, ed T. Cebeci (Butterworth-Heinemann) ch 4, pp 89–153
- [55] Ubbink O. 1997 Numerical prediction of two fluid systems with sharp interfaces *PhD Thesis* University of London